Cell Reports
Methods

Article

Extracting electromyographic signals from multi-channel LFPs using independent component analysis without direct muscular recording

Graphical abstract

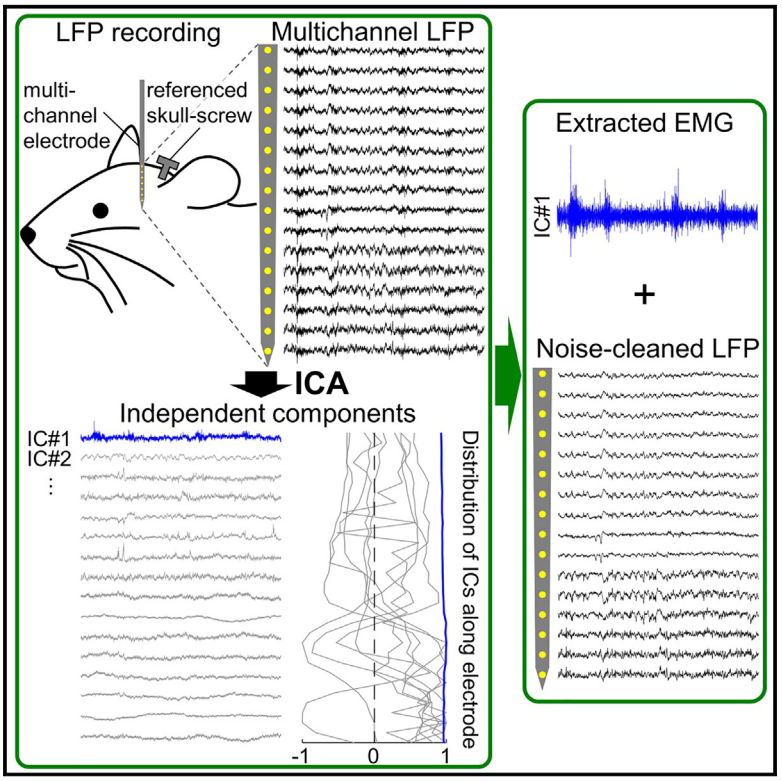

Highlights

- EMG signals can be extracted from LFP signals without direct muscular recording
- The extracted signal is highly correlated with direct EMG recording signals
- The extracted signal is useful in measuring animal behaviors as well as actual EMG
- This method contributes to precise and stable long-term behavior measurement

Authors

Hisayuki Osanai, Jun Yamamoto, Takashi Kitamura

Correspondence

takashi.kitamura@utsouthwestern.edu

In brief

Osanai et al. demonstrate that electromyography (EMG) signals can be extracted from multichannel local field potential (LFP) recordings using the blind source separation technique without direct measurement of muscle activity. The method adds precise and long-term behavioral measurements with EMG information in wide-ranging *in vivo* electrophysiology experiments.

Osanai et al., 2023, Cell Reports Methods *3*, 100482
June 26, 2023
https://doi.org/10.1016/j.crmeth.2023.100482

CellPress

Cell Reports Methods

CellPress
OPEN ACCESS

Article

Extracting electromyographic signals from multi-channel LFPs using independent component analysis without direct muscular recording

Hisayuki Osanai,[1] Jun Yamamoto,[1] and Takashi Kitamura[1,2,3,*]
[1]Department of Psychiatry, University of Texas Southwestern Medical Center, Dallas, TX 75390, USA
[2]Department of Neuroscience, University of Texas Southwestern Medical Center, Dallas, TX 75390, USA
[3]Lead contact
*Correspondence: takashi.kitamura@utsouthwestern.edu
https://doi.org/10.1016/j.crmeth.2023.100482

MOTIVATION Electromyography (EMG) has been used to assess animal behaviors such as sleep/wake states and freezing behavior. However, despite the benefits of accurate behavior assessment, EMG is often not obtained together with brain activity recording because it requires additional surgery and setups. In addition, a high risk of EMG electrode breakage hampers long-term EMG recording experiments. In this study, we demonstrate that EMG signals can be extracted from multichannel local field potential (LFP) data using the blind source separation technique without direct measurement of muscle activity.

SUMMARY

Electromyography (EMG) has been commonly used for the precise identification of animal behavior. However, it is often not recorded together with *in vivo* electrophysiology due to the need for additional surgeries and setups and the high risk of mechanical wire disconnection. While independent component analysis (ICA) has been used to reduce noise from field potential data, there has been no attempt to proactively use the removed "noise," of which EMG signals are thought to be one of the major sources. Here, we demonstrate that EMG signals can be reconstructed without direct EMG recording using the "noise" ICA component from local field potentials. The extracted component is highly correlated with directly measured EMG, termed IC-EMG. IC-EMG is useful for measuring an animal's sleep/wake, freezing response, and non-rapid eye movement (NREM)/REM sleep states consistently with actual EMG. Our method has advantages in precise and long-term behavioral measurement in wide-ranging *in vivo* electrophysiology experiments.

INTRODUCTION

While neural correlates of animal behavior are examined most frequently with video observation of an animal's movement, physiological signals such as electromyography (EMG) are also often used to monitor the small movements of the animal that can be missed in video observation. In neuroscience studies, EMG has been used to accurately assess sleep/wake states[1–6] and freezing behavior.[7–9] However, despite the benefits of accurate behavior assessment, EMG is often not obtained together with brain activity recording because it requires additional surgery and setups.[7,10–13] Furthermore, in the case of implanting a silicon probe, most commercial headstage preamplifiers are not designed with extra pins to obtain EMG signals, thus an additional preamplifier is required, which increases the total implant weight, potentially interfering with the normal behavior of small animals such as mice. Moreover, a high risk of EMG electrode wire breakage during experiments[14–16] hampers long-term experiments.

Field potentials have been shown to be correlated with an animal's behaviors such as sleep/wake conditions[1,2,17–20] and fear freezing behavior.[8,21,22] Field potential signals are often electrically referenced to one of the electrodes placed in a brain to suppress excessive common noise generated from the outside of the brain.[19,23–25] On the other hand, because the field potential signals can be distorted by the electrical signals at the reference electrode site,[24–26] an electric reference is frequently set outside of the brain (e.g., a skull screw).[27–29] In this case, in order to minimize the noise arising from the distal reference electrode setting, multiple methods have been proposed such as common average reference,[30] current source density analysis,[31–33] and application of independent component analysis (ICA).[34]

ICA is a blind source separation technique that isolates temporally independent source signals.[35–38] This technique has been

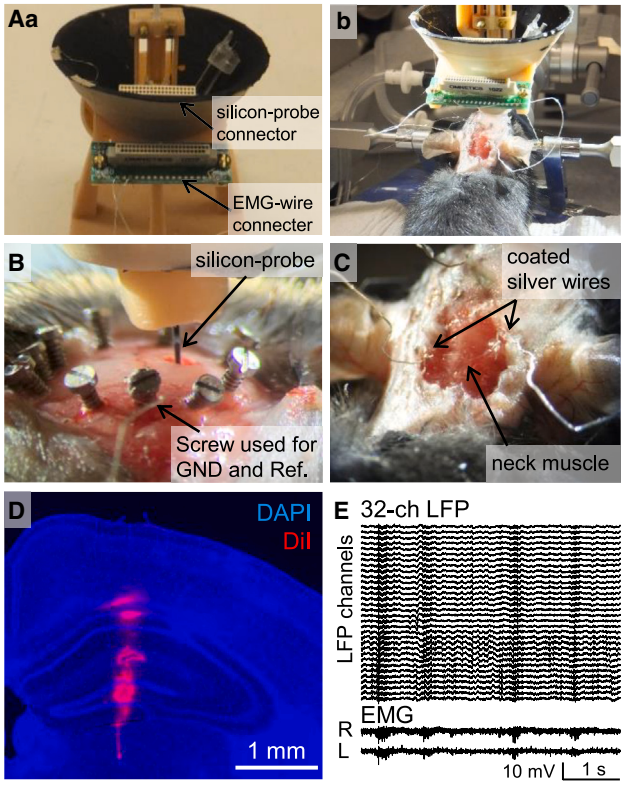

Figure 1. LFPs and EMG recording setups

(A) A microdrive system for implanting a silicon probe and EMG electrode wires, placed on a jig (a) and during surgery (b).

(B) Skull screw used for an animal's ground and reference. The silicon probe was inserted into the brain in this picture.

(C) EMG electrode wire placements. The tips of the coated wires were exposed and looped into the left and right neck muscles.

(D) The trace of silicon probe implantation into hippocampus. The probe was coated with DiI before implantation.

(E) Representative LFP traces from a 32-ch silicon probe referencing the skull screw (top), and right (R) and left (L) neck EMG traces (bottom).

well established for decades in "denoising" recorded neural signals by isolating and deleting the noise components from the field potential data, in which EMG artifacts are considered to be a major noise source.[34,39–43] However, although the putative EMG component isolated by ICA has been the target of noise suppression, it has not yet been investigated to what extent this component correlates with real EMG signals. Thus, the component has not been proactively used as a measurement of animals' behavioral states.

Here, we hypothesize that ICA can reconstruct EMG signals from multichannel local field potential signals obtained by a silicon probe or tungsten wire electrodes without direct measurement of muscular signals. To investigate the correlation between IC and EMG signals, we simultaneously implanted a silicon probe into a mouse's hippocampus and wire electrodes into the neck muscles. Local field potentials (LFPs) were recorded electrically referenced to a skull screw over the cerebellum. Next, we obtained ICs from the LFPs using ICA and demonstrated that EMG-like high-frequency components (IC-EMG) could always be obtained from the LFPs. These components were shown to highly correlate with directly measured EMGs. We further demonstrated that this IC-EMG can be used to measure sleep/wake activity and freezing behavior. Finally, we demonstrated that IC-EMGs can also be obtained from four-channel multisite brain-area LFPs obtained by tungsten wire electrodes.

RESULTS

IC-EMG is highly correlated with real EMG signals

LFP signals were obtained from a 32-channel silicon probe implanted in the mouse hippocampus, using a skull screw for electric reference above the cerebellum (Figures 1A–1D). At the same time, EMG signals were obtained from the left and right neck muscles (Figures 1C and 1E). The ICs were obtained by ICA from the recorded multichannel LFP signals (Figure 2A). Figure 2Ab illustrates one of the obtained ICs (IC#1) showing EMG-like higher frequency activity than other ICs. The back-projected reconstructed signals on the original channels using this IC showed that the signals distributed uniformly along the channels (Figure 2Ba). Deleting this IC clarified the weaker and slower activities, which had been previously contaminated with the noise-like large high-frequency activity in the original waveforms (Figure 2Bb). Indeed, IC#1 showed a clear peak between 100 and 200 Hz in the estimated power spectrum density (Figure 2C), and the weight distribution of this component was highly uniform compared with other ICs (Figure 2D). In LFP data obtained from ten mice, only one IC showing uniform weight distribution (standard deviation [SD] < 0.1) was consistently obtained from individual mice (Figure 2Ea). To focus on uniformly distributed ICs, we classified ICs having a minimum SD among ICs obtained in individual mice and an SD <0.1 as a uniform IC. The uniform IC also showed the maximum mean value of its weight distribution and tended to have large amplitude activities (Figure 2Eb; uniform IC vs. other ICs: weight mean = 0.97 ± 0.007 vs. 0.21 ± 0.013, $t_{(265)}$ = 10.99, p = 2.15e−23; weight SD = 0.019 ± 0.003 vs. 0.36 ± 0.009, $t_{(265)}$ = −7.44, p = 1.42e−12; amplitude ratio = 0.88 ± 0.090 vs. 0.20 ± 0.013, $t_{(265)}$ = 9.88, p = 8.35e−20, respectively). In addition, the uniform IC always had a peak frequency between 100 and 200 Hz, similar to the real EMG power spectrum density (Figure 2F), indicating that the uniform IC reflected EMG signals.

We next investigated to what extent the uniform IC correlates with real EMG signals. Figure 3A illustrates the filtered signals of uniform IC and the real EMG, and Figure 3B shows the time course of their amplitudes calculated by root mean square (RMS) with 100 ms time windows. As we expected, the uniform IC and the real EMG signals were highly correlated, with correlation coefficients that were more than 0.9 (Figures 3C and 3D). Therefore, EMG signals can be reconstructed from skull-screw-referenced multichannel LFP data by ICA without direct EMG recordings. These signals are represented by the uniform IC, which hereafter we termed IC-EMG.

The EMG-like components were not obtained from brain-referenced LFPs in most cases (eight out of ten mice) since EMG information was absent due to subtraction (Figures S1A–S1C). We

CellPress
OPEN ACCESS

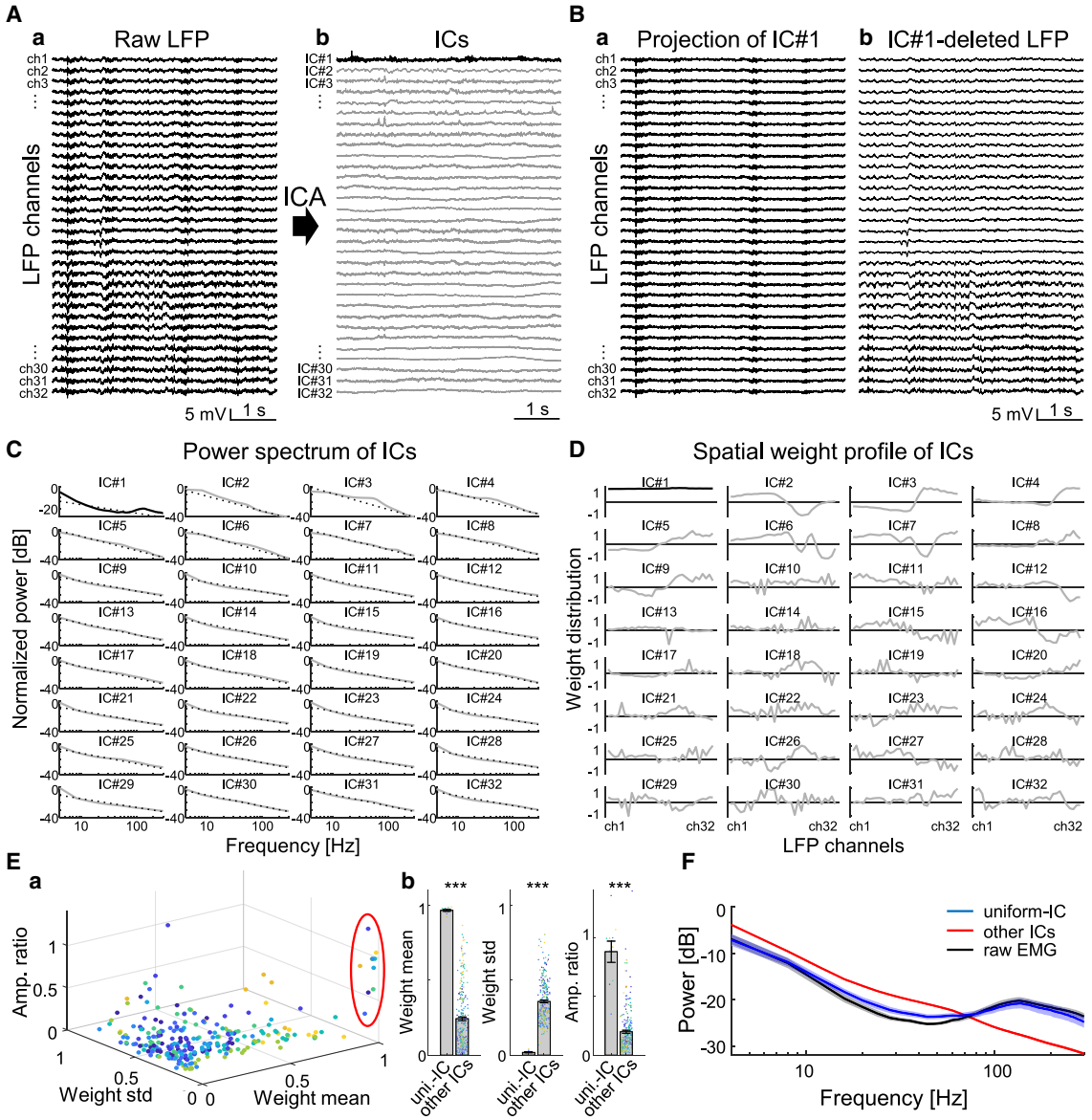

Figure 2. Identification of putative EMG component from LFP by ICA

(A) Raw LFP traces (a) and their independent components (ICs) separated by ICA (b). Note that IC#1 (black trace) showed higher frequency activity than other ICs (gray traces), similar to the EMG traces in Figure 1E.

(B) Projection of IC#1 to the original LFP channels (a). The cleaned LFP obtained by deleting IC#1 from the raw LFP (b). The EMG-like high-frequency activities disappeared in IC#1-deleted LFP.

(C) Log-log plots of the normalized power spectrum densities of each IC shown in (A). IC#1 showed peak power at the range >100 Hz. Black dotted lines indicate the power of aperiodic exponent (see STAR Methods).

(D) The weight distribution of ICs shown in (A). IC#1 had the most uniform (minimum standard deviation [SD]) distribution.

(E) (a) Scatterplot of IC's mean weight, SD, and amplitude (see STAR Methods) obtained from ten mice. Red circle indicates the ICs classified as uniform IC in each mouse. (b) Averaged parameters of IC-EMGs and other ICs. Dots of each color indicate different mice (mean ± standard error [SE]; ***, $p < 0.001$).

(F) Averaged normalized power spectral density of the uniform IC (blue) other ICs (red), and raw EMG (black).

observed the EMG-like components from the brain-referenced LFPs only when the noise level of LFPs was different between the recording channels such that brain referencing could not completely reduce the noise (Figures S1D–S1F and S2). Thus, brain-referenced LFP is not ideal for obtaining EMG signals using ICA.

IC-EMG provides behavior measurements

Next, we examined whether the IC-EMG is useful for annotating animals' behavioral states. Mice were placed into and allowed to move freely in the open field chamber (Figure 4A). LFPs and EMGs were recorded while the mice were in the chamber (Figure 4B), together with video tracking of the animals' positions.

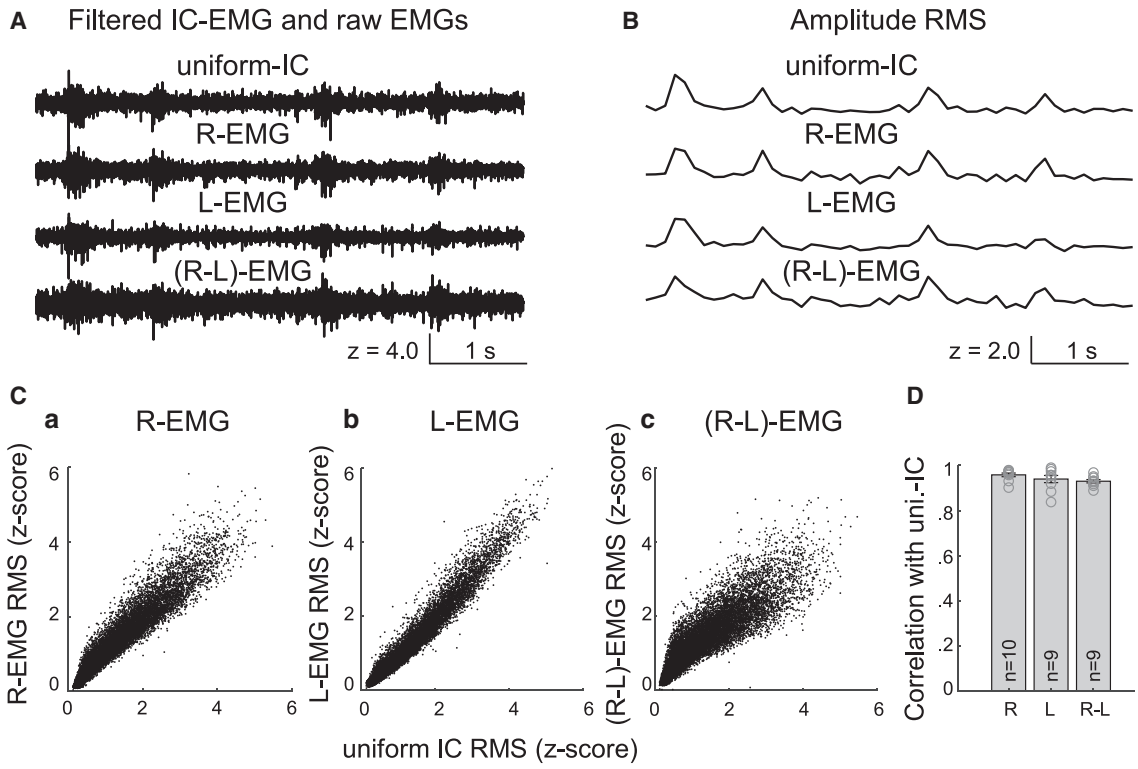

Figure 3. Correlation of uniform IC and raw EMG signals

(A) 50–500 Hz filtered waveforms of uniform IC (IC#1 in Figure 2), right-neck EMG (R-EMG), left-neck EMG (L-EMG), and Δ(right-to-left) EMG ([R-L]-EMG) which is obtained by subtracting L-EMG from R-EMG to remove the effect of the common reference (skull-screw reference).

(B) Root mean square (RMS) with 100 ms bin time windows of each trace in (A).

(C) Correlation of uniform IC with each EMG, (a) with R-EMG, (b) L-EMG, and (c) (R-L)-EMG. (R-L)-EMG is less correlated with IC-EMG than R- or L-EMG because the common reference effect is absent due to the subtraction, but still shows high correlation.

(D) Average Pearson's correlation coefficient of uniform IC and real EMG from ten mice. L-EMG data from one mouse are missing due to the wire break during experiments. Correlation between uniform IC and R-EMG = 0.96 ± 0.008, L-EMG = 0.94 ± 0.016, (R-L)-EMG = 0.93 ± 0.007 (mean ± SE).

We categorized animal behavioral states from the video into sleep, quiet awake (QAW), and active, classified according to the animals' average head speed (Figure 4C; see STAR Methods). Amplitudes of IC-EMG and real EMG were quantified in ten mice during each behavioral state. Figure 4D shows that there were significant differences in the IC-EMG amplitudes, similar to the real EMG, between sleep, QAW, and active behavioral states (Figure 4D).

Freezing behavior has been demonstrated as an indicator for fear response in both innate and conditioned reactions.[44–47] We furthermore demonstrate that IC-EMG is useful for fear freezing detection, consistent with the previous studies showing that EMG can be used as a measure of fear freezing behavior.[7] Mice were conditioned in the tone fear conditioning paradigm while their fear freezing was recorded with video observation, along with LFPs and real EMG signals (Figure 5A). For conditioning, mice were exposed to three pairings of a 20 s tone and a 2 s foot shock on day 1. Then, fear freezing behaviors in response to tone were monitored on day 2 in a different context and scored by the animal's motion in the recorded video. At the same time, IC-EMG was obtained from the recorded LFPs and the amplitudes of IC-EMG and real EMG were examined while animals showed freezing and non-freezing behavior (Figure 5B). The mice actively explored the recording box before the tone delivery, while they showed increased freezing behaviors after the first tone delivery (Figures 5B and 5C). From the LFP data of five mice, IC-EMG showed a significantly lower amplitude during the freezing state compared with the non-freezing state, similar to the results of real EMG signals (Figure 5D). Together, these results demonstrated that IC-EMG is useful for annotating animal behavior such as sleep/QAW/active behavioral states and freezing/non-freezing states.

IC-EMG can improve precise REM sleep detection

We examined whether the IC-EMG is useful for precise annotation of the rapid eye movement (REM) sleep stage. REM/non-REM (NREM) sleep periods are often classified by a high/low theta-to-delta ratio of field potential when the animal shows stationary behavior.[48,49] However, because many factors can increase theta power during QAW[8,21,22,50–55] (see discussion), the combination only of video recording and field potential recording has difficulty in fine discrimination of QAW and REM sleep stats. The most established sleep scoring method uses a combination of field potential and EMG.[56–60] In this paradigm, sleep/wake are

CellPress
OPEN ACCESS

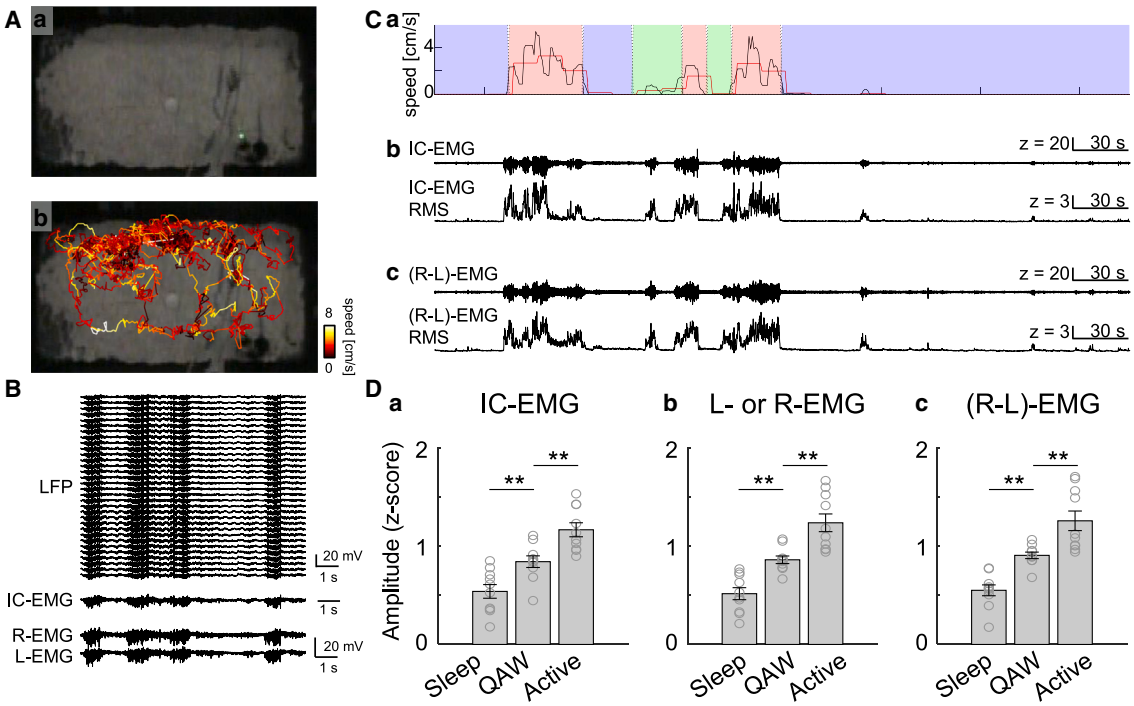

Figure 4. IC-EMG can provide measurements of animal behaviors

(A) The recording chamber (a) and head position tracing (b) during LFP and EMG recording.

(B) Simultaneous recording of LFP and EMG when the mouse was freely moving in the recording chamber. EMG-IC was obtained from raw-LFP by ICA.

(C) Speed of the animal's head, traces of IC-EMG and raw EMG, and their amplitudes at the same time. (a) Head position speed (black line) and its average during each 15 s epoch (red line), (b) *Z* scored IC-EMG and its RMS amplitude, and (c) *Z* scored raw EMG and its RMS amplitude. Animal behavior was categorized into sleep (blue), quiet awake (QAW; green), and active (red) based on the video data.

(D) Amplitude of IC-EMG (a, n = 10), L- or R-EMG (b, n = 10), and (R-L)-EMG (c, n = 9) during different animal behaviors. Amplitudes between sleep vs. QAW vs. active: IC-EMG, 0.54 ± 0.070 vs. 0.84 ± 0.060 vs. 1.17 ± 0.071, p = 0.010 (sleep/QAW) and p = 0.005 (QAW/active); L- or R-EMG, 0.52 ± 0.061 vs. 0.86 ± 0.039 vs. 1.24 ± 0.090, p = 0.003 (sleep/QAW) and p = 0.001 (QAW/active); (R-L)-EMG, 0.55 ± 0.055 vs. 0.91 ± 0.033 vs. 1.26 ± 0.100, p = 0.003 (sleep/QAW) and p = 0.003 (QAW/active) (mean ± SE).

classified by low/high amplitude EMG activities in addition to the animal's movements in the recorded video. Here, we demonstrate that IC-EMG can be used for sleep scoring similarly to real EMG recording.

LFPs and EMGs of the mice were recorded in the open field chamber or their home cages (Figure 6A). The animals' behaviors were first annotated with the video tracking of the animals' positions (Figure 6Aa). High theta- (6–9 Hz)-to-delta (0.1–4 Hz) ratio periods were observed while the mice were stationary (Figures 6Ab and 6Ac). In order to separate REM sleep periods from the QAW state, the animal behaviors were further classified using IC-EMG information that the stationary periods with high IC-EMG amplitudes were re-categorized as being in the awake state (QAW) (Figure 6Ad), similar to the use of the EMG (Figure 6Ae). Then, REM/NREM/QAW states were annotated with the combination of the theta-delta ratio and the animal's speed or the combination of the theta-delta ratio, the animal's speed, and the IC-EMG or the EMG (Figure 6B). Some periods annotated as REM based only on the video (Figure 6Ba) were categorized into QAW when the annotation was based on IC-EMG (Figure 6Bb), similar to the result based on the EMG (Figure 6Bc), because of their large amplitudes of muscular activities during the periods which are not likely to occur during sleeping states.

The dynamics of IC-EMG and EMG during IC-EMG- and EMG-based categorized REM periods were consistent with previous studies where EMG shows silent and occasional twitch activities[61,62] and that body movement occurs at the end of REM.[63] To evaluate the extent to which the quality of the video-based and the IC-EMG-based state classifications is close to the EMG-based method, the REM sleep periods were detected from six silicon-probe-implanted mice (Figure 6C). Because the sleep periods were more strictly annotated, the IC-EMG-based method showed less false-positive rates of REM detection compared with the video-only-based method (Figure 6Da; video: 1.18% ± 0.38%, $t_{(5)}$ = 3.13, p = 0.025; IC-EMG: 0.39% ± 0.20%, $t_{(5)}$ = 1.98, p = 0.104, one-sample t test with zero), and negligible levels of false-negative rates in IC-EMG (0.16% ± 0.12%, $t_{(5)}$ = 1.27, p = 0.260, one-sample t test with zero). Also, the IC-EMG-based REM period detection was similar (Cohen's kappa[64–66]) to the EMG-based method, while the similarity of the video-only-based method was less (Figure 6Db; video: 0.91 ± 0.03, $t_{(5)}$ = −2.89, p = 0.035; IC-EMG: 0.96 ± 0.02, $t_{(5)}$ = −1.93, p = 0.112, one-sample t test with kappa = 1). Therefore, the use of IC-EMG improves precise REM sleep detection similarly to the use of real EMG by decreasing false-positive REM periods.

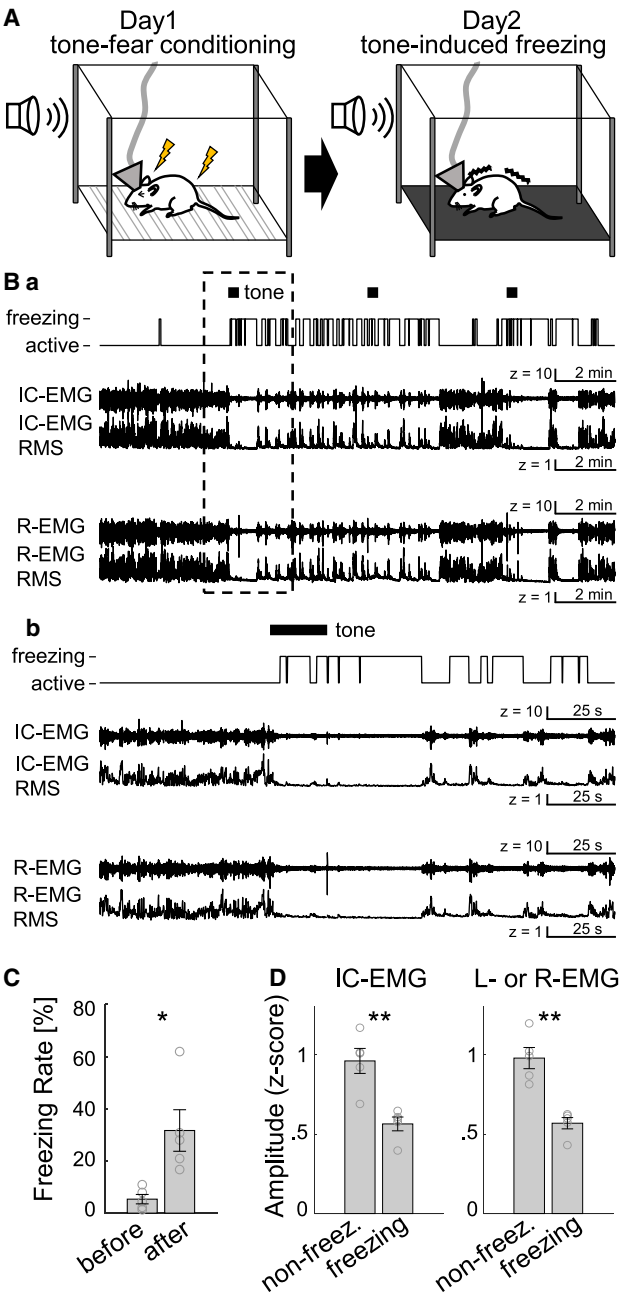

Figure 5. IC-EMG can be measurements of animal's fear freezing

(A) Schema of the tone fear conditioning task.

(B) Animals' freezing behavior at day 2, IC-EMG and raw EMG traces, and their RMS amplitudes during whole sessions (a) and 1 min before and after the tone onset (b).

(C) Freezing rate during habituation session and test sessions (n = 5) before and after the first tone delivery. Freezing rate before vs. after the tone = 5.4% ± 1.8% vs. 31.7% ± 8%, respectively, $t_{(8)} = -3.22$, p = 0.012 (mean ± SE).

(D) Amplitude of IC-EMG and L- or R-EMG during animal's active/freezing states. (R-L)-EMG was not analyzed because one side of the EMG wires was broken during foot-shock delivery in three out of five mice. The *Z* scored amplitudes during non-freezing and freezing states: IC-EMG, 0.96 ± 0.079 vs. 0.56 ± 0.043, $t_{(8)} = 3.65$, p = 0.007; EMG, 0.98 ± 0.067 vs. 0.57 ± 0.036, $t_{(8)} = 3.37$, p = 0.001, respectively (mean ± SE).

IC-EMG can be obtained from multisite brain-area recording

Finally, we examined whether IC-EMG can be obtained from multisite brain-area recording data. We have previously recorded four channel LFPs in the anterior cingulate cortex (ACC), the basolateral amygdala (BLA), white matter (WM) of the dorsal CA1, and the ventral CA1 of mice.[69] We had obtained the LFP signals referenced to the skull screw over the cerebellum, and ICs were separated by ICA from the recorded LFPs into ICs (Figures 7A–7D). Similar to the case of silicon-probe recordings (Figure 2), one of the ICs consistently present in each of the four mice exhibited a highly uniform weight distribution (Figures 7E and 7G). These components also showed a peak frequency between 100 and 200 Hz (Figures 7F and 7H), which is consistent with the results of silicon-probe recordings (Figure 7F), indicating a strong correlation with actual EMG signals. We examined the amplitude of IC-EMG when the mice explored the open field chamber. Again, consistent with the results of silicon-probe recordings, IC-EMG amplitudes were significantly higher during awake states than sleeping states (Figure 7I). We finally examined IC-EMG amplitudes during freezing/non-freezing behaviors during the observational fear.[70–72] The recorded mouse, as an observer, and his cagemate, as a demonstrator, were placed into the two chambers separated by a transparent plexiglass partition. On the recording day, the foot shock was delivered to the cagemate demonstrator, which produced the observational fear response[69] (Figure 7Ja). During the freezing period, IC-EMG of 4-channel LFP showed significantly lower amplitudes compared with the non-freezing state in the observer (Figure 7Jb). Therefore, IC-EMG can also be obtained from multisite brain-area LFP recording, and it provides behavior measurement of sleep/awake states and fear-freezing/non-freezing states. Moreover, these results also demonstrate that our method is able to reconstruct EMG signals from data obtained in the past so long as an electrical reference was set on the animal's skull screw.

DISCUSSION

Although previous works have shown good performance of ICA in the reduction of EMG-like artifacts from field potential data, evidence of to what extent the separated component and the actual EMG signal correlate was lacking. Thus, no prior attempt was made to use this EMG-like component proactively. The current study has shown that the EMG component obtained from multichannel LFP signals by ICA is highly correlated with actual EMG signals. The IC-EMG was further demonstrated to be useful for measuring animals' sleep/wake and fear-freezing behavior as well as actual EMG. We also showed that EMG component separation could also be performed by ICA with multisite brain-area LFP recording. Therefore, the current study demonstrated that the EMG signal can be reconstructed from multichannel LFP by ICA without any additional surgery or setup, which can be helpful in the measurement of animal behaviors. In addition, our method allows re-examining animal behaviors in previously obtained LFP data.

CellPress
OPEN ACCESS

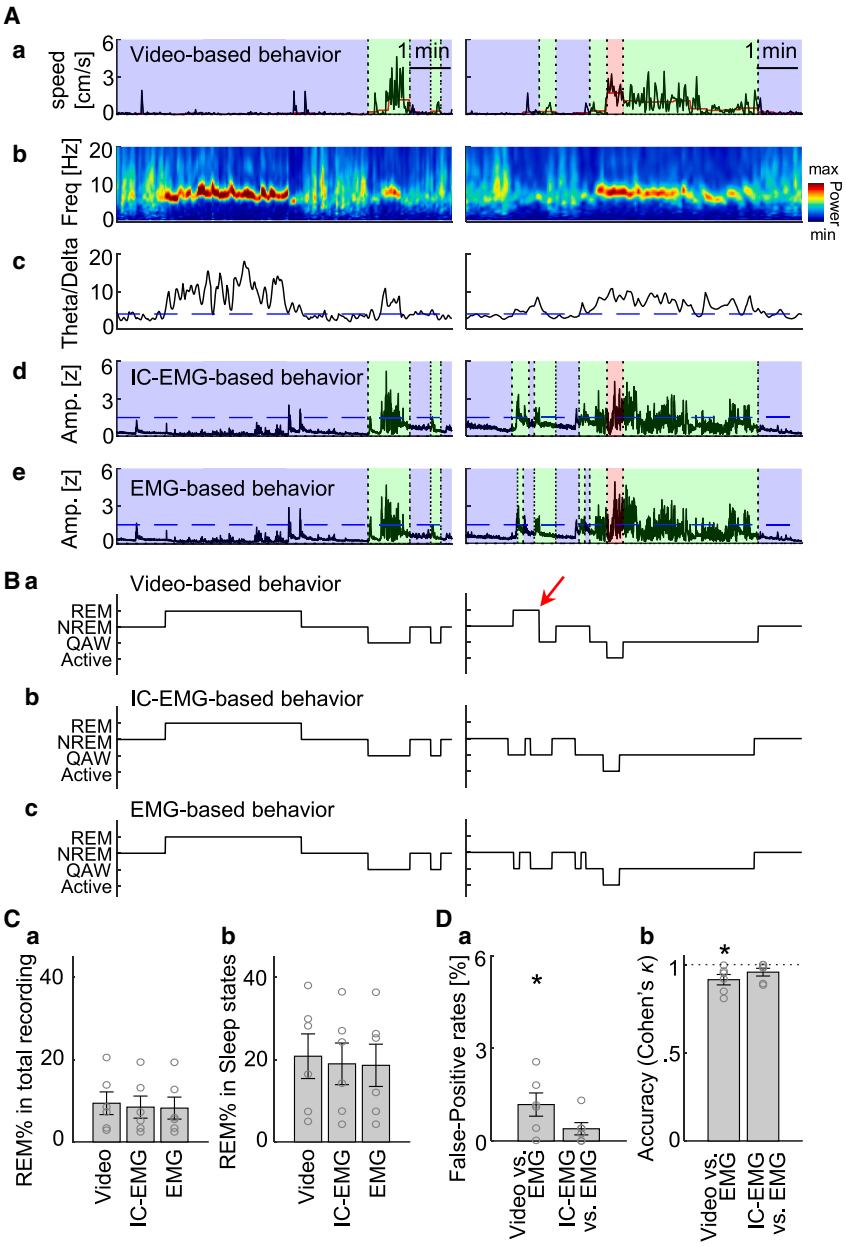

Figure 6. IC-EMG is useful for precise annotation of REM sleep scoring

(A) Sleep/wake annotation based on the video recording, IC-EMG, and EMG. (a) Head position speed (black line) and its average during each 15 s epoch (red line). Animal behavior was categorized into sleep (blue), QAW (green), and active (red) based on the head speed. (b) Spectrogram of LFP at stratum lacunosum-moleculare layer of CA1. (c) Trace of theta (6–9 Hz)-to-delta (0.1–4 Hz) ratio. Blue dotted line indicates ratio = 4. (d and e) Sleep states categorized based on video recording (a) were re-annotated into QAW if the amplitudes of the *Z* scored IC-EMG (d) and (R-L)-EMG (e) are high (see STAR Methods). Black lines indicate RMS amplitudes of IC-EMG/(R-L)-EMG. Blue dotted lines indicate z = 1.5.

(B) Sleep scoring based on the video recording (a), IC-EMG (b), and (R-L)-EMG (c). The states were classified into REM when the theta-to-delta ratio was ≥4 during sleep state (see STAR Methods). Red arrow indicates that the REM period, which is categorized based on the video, was re-categorized as wake by IC-EMG- and EMG-based annotation due to their high amplitudes.

(C) REM sleep duration from the six mice in the total recording time (a) (percentages based on video vs. IC-EMG vs. EMG, 9.38 ± 2.75 vs. 8.44 ± 2.68 vs. 8.21 ± 2.67) and in total sleep periods (b) (percentages based on video vs. IC-EMG vs. EMG, 20.80 ± 5.42 vs. 18.95 ± 5.06 vs. 18.59 ± 5.13). These amounts are consistent with previous reports.[67,68] (mean ± SE).

(D) The agreement of REM sleep scoring based on video and IC-EMG vs. the scoring based on EMG; false-positive rates (a), and Cohen's kappa values (b) (mean ± SE; *, $p < 0.05$).

Advantages of IC-EMG

Although techniques used for EMG signal acquisition are simple, simultaneous recording of EMG with brain activity is not a trivial matter because it requires additional surgeries and setups, as we described in the introduction. In the current study, the total microdrive weight used for silicon probe implant and EMG recording was 6.5 g, while the weight would be reduced to 4.7 g in the case that EMG recording was not needed because the electrical interface board for EMG preamp can be removed. We did not observe abnormal behaviors in the adult mice used in this study, but the increased implant weight could interfere with the behavior of more juvenile animals. Stable EMG recording has also been a challenging problem, as the recording wires need to remain attached to the animal despite the mechanical stress caused by muscular movements. In our experiments, three out of twelve mice broke the wires; one mouse broke one side of the EMG wires within a week after the surgery, and another two mice broke one side of the wires while receiving fear conditioning foot shocks. Reconstructing EMG signals from LFP using ICA does not require a wire electrode implant. The ground/reference wire used for the LFP recording connected to the skull screw was fully covered with dental acrylic and did not receive mechanical stress after surgery, ensuring stable recording. Therefore, our IC-EMG method not only reduces the requisite effort of additional surgery and setup preparation for EMG recording but also enables stable simultaneous recording of EMG and LFP with freely moving animals, which allows long-term behavior experiments without the risk of a wire break.

Up to now, several methods have been proposed to score animal behaviors without EMG. Video-based sleep scoring has been shown to have a high correlation with EMG-based scoring.[73,74] The video-based methods, however, have a

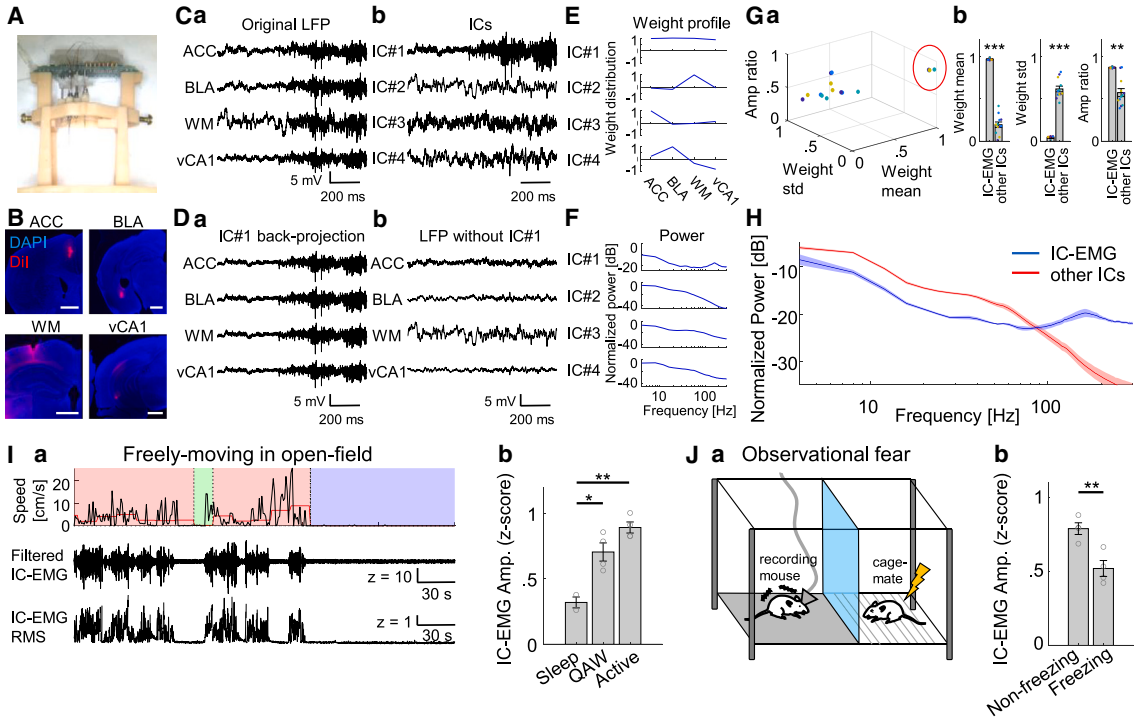

Figure 7. IC-EMG can be obtained from multisite brain-area recording

(A) Implant device on jig equipped with 4-ch tungsten wire electrodes.

(B) The electrode traces. The electrodes were coated with DiI before implantation. Scale bar: 1 mm.

(C) Representative LFPs from 4-ch electrodes (a), and their ICs (b). The LFP signals were referenced to the skull screw.

(D) The back-projected field potential from IC#1 (a), and the cleaned LFP waveforms obtained by deleting IC#1 LFP from the raw LFP (b).

(E) Weight distribution of ICs.

(F) Power spectrum density of ICs.

(G) Scatterplot (a) and bar plots (b) of IC's mean weight, SD, and amplitude ratio obtained from four mice. Red circle indicates the uniform ICs (IC-EMG) in each animal. Averaged parameters were IC-EMG vs. other ICs: weight mean = 0.96 ± 0.007 vs. 0.20 ± 0.033, $t_{(14)}$ = 13.31, p = 2.45e−9; weight SD = 0.045 ± 0.011 vs. 0.62 ± 0.033, $t_{(14)}$ = −9.69, p = 1.37e−7; amplitude ratio = 0.87 ± 0.005 vs. 0.57 ± 0.047, $t_{(14)}$ = 3.53, p = 0.003, respectively (mean ± SE).

(H) Average power spectrum density of the IC-EMG (blue) and other ICs (red).

(I) IC-EMG from freely moving animals. Speed of animal's head position (top), 50–500 Hz filtered IC-EMG (middle), and RMS amplitude of IC-EMG (bottom). (b) Average amplitude of IC-EMG from four mice. Amplitudes between sleep vs. QAW vs. active: 0.32 ± 0.042 vs. 0.70 ± 0.070 vs. 0.89 ± 0.042, p = 0.013 (sleep/QAW) and p = 0.0014 (sleep/active).

(J) IC-EMG during the observational fear task. (a) Schema of the task, and (b) IC-EMG amplitude during animal's active and freezing states. The *Z* scored amplitudes during non-freezing and freezing states: 0.79 ± 0.040 vs. 0.52 ± 0.054, $t_{(6)}$ = 4.03, p = 0.007 (mean ± SE).

drawback in identifying the fine sleep structures because they take 40 s of immobility as a threshold to define sleeping, while short sleep bouts of less than 20 s have been reported in sleep-deprived rodents[75] and of excessive sleepiness in humans.[76,77] Video recording systems complemented with infrared beam breaking,[78] piezoelectric signals,[79,80] and respiration measurement[77] were also proposed; however, these again require additional experimental setups. Sleep has also been often determined based on the oscillatory power of LFP or EEG combined with video tracking without EMG. In these cases, active awake and REM sleep are identified by prominent theta oscillation (6–9 Hz), while slow-wave sleep is characterized by increased delta oscillation (<4 Hz)[48,49,81] and by the appearance of sharp wave ripple and cortical spindles.[20,82,83] Another study further distinguished sleep and QAW states using a criterion that delta power is increased during slow-wave sleep compared with QAW state.[84] However, there is still a limitation of this approach in fine state discrimination of immobility states. Although theta is prominent during REM sleep, theta power during QAW can also increase with many factors including respiration,[50] vestibular stimulation,[51] sleepiness,[52] fear,[8,21,22] attention, and other cognitive functions.[53–55] In addition, QAW theta becomes less prominent during waking immobility, eating, grooming, and defecation.[53,85] Also, QAW delta power is reported to increase prior to the wake-to-slow-wave-sleep transition onset.[86,87] Thus, EEG-based behavior classification has difficulty in fine discrimination of QAW, slow-wave sleep, and REM sleep. IC-EMG provides the benefit of precise animal state discrimination compared with other conventional methods without utilizing EMG information.

While we demonstrated that IC-EMG can be a measure of sleep/wake and fear-freezing behavior, we also observed that its amplitude was increased during water licking, food chewing, and grooming behavior. Thus, IC-EMG has the potential to be a

measure of various animal behaviors, although further investigation is needed to clarify to what extent animal behavior types can be scored by IC-EMG.

In this study, we obtained EMG signals from LFP data by ICA. The same methodology has the potential to be applied to EEG research, considering that ICA has been a well-established method to eliminate EMG artifacts from EEG data. Recently, several source separation techniques, including empirical mode decomposition,[88,89] an improved version of ICA-based separation,[90] and others,[91–94] have been proposed to have better noise reduction quality for EEG data than conventional ICA, with the condition of fewer recording channels. Therefore, utilization of these signal source separation techniques would be possible to improve the quality of EMG signals isolation from EEG data.

Signal source of IC-EMG

We obtained IC-EMG from the multichannel LFP signals, which were characterized to have uniform IC weight distribution. Considering neural activity factors surrounding the electrode should contribute to LFP in a more localized manner,[24,95] the signal source of a such uniform distribution component is supposed to be distal volume conduction[96] or a common electrical reference.[34] However, the volume conduction factor is less likely to be the main factor of IC-EMG. First, IC-EMG has a peak power at 130–140 Hz, while power line conduction should generate a peak at a lower frequency range. Second, such a high-frequency neural event in a brain corresponds to a sharp wave ripple,[20] but it is unlikely to be generated from a uniformly distributed source, and its amplitude should be smaller than other slower oscillatory activities. Thus, although both signals were possibly separated by ICA, we assume that the major factor of that uniform component is the electrical reference. In this study, we used the skull screw over the cerebellum as an electrical reference, which can pick up both signals of muscle activities near the screw and cerebellar activity. However, although the precise contribution of cerebellar EEG is unclear, it is reported that overt activity is not seen in a healthy rodent brain.[97] Together with the high correlation with neck EMG, we assume that the head-neck muscular activities surrounding the electrically referenced skull screw are a major signal source of IC-EMG.

Factors that may affect IC-EMG identification

In our method, the high-noise-level channels identified by eye were removed prior to running ICA. Such noisy signals can be caused by the degradation of the silicon probe electrode that leads to crosstalk between channels[98] and changes in the frequency-impedance characteristics,[99,100] which have a risk of skewing the time course of LFP traces. Because ICA is a technique to separate temporally maximal independent waveforms, the skewed LFP can generate additional components for which a signal source actually does not exist. Indeed, although only one IC-EMG component was obtained from each mouse in the current study after the removal of bad channels, we have observed two uniform components correlated with EMG (mean weight = 0.97 and 0.95, mean SD = 0.02 and 0.03, amplitude [Amp] ratio = 0.65 and 0.46, correlation coefficient = 0.97 and 0.97, respectively) from one mouse when we did not remove the channels of high noise level before the ICA computation. Thus, including unhealthy electrode site signals in ICA may generate "ghost" components, although EMG signals can still be reconstructed from the LFPs.

Benefits of using ICA for reducing noise arising from outside-brain reference electrode setting

In this study, it was demonstrated that ICA can separate muscle activities from multichannel LFP data with a skull screw electric reference. Another advantage of applying ICA to LFP data is that, as we demonstrated in Figure 2Bb, it can obtain noise-cleaned LFP data against a brain-external reference.

There have been multiple methods for reducing the noise arising from the distal reference electrode, which is set to avoid the signal distortion caused by placing the reference electrode close to the recording site. Common average reference is the method to generate a more ideal reference by averaging all the recordings on every electrode site to use as a reference.[30] While the ideal reference can be obtained if the average produces near-zero activity, the average does not often produce zero, especially in the case of recording from the local brain area because neural activities at each recording channel are supposed to be correlated with each other. Current source density analysis has also been widely used as a reference-independent measure that estimates the strength of extracellular current generators,[31–33] which is conducted by calculating a second spatial derivative of the recorded potentials between neighboring electrodes in the standard method. However, because the spatial noise is amplified through the differentiation, it often requires spatial filtering,[101–103] which decreases spatial resolution of LFP signals. In addition, this method is not useful in the case of certain recording electrode setups, such as those using tungsten wire electrodes, or in the case of multibrain-site recording because it requires precise electrode site distance information. The ICA-based method, on the other hand, does not depend on the electrode locations, and subtracting electrical reference activity can be interpreted as re-referencing to a zero-activity location.[34] Thus, our method to use ICA to LFP data does not only have an advantage in extracting EMG activities without an EMG electrode implant but also in obtaining noise-reduced LFP signals, avoiding the potential signal distortion that is encountered in the case of a within-brain reference electrode placement.

Conclusion

This study certified that EMG signals can be reconstructed from multichannel LFP signals by ICA. Thus, our method provides a physiological measure of animal behavior in LFP data without the extra effort of direct EMG recording. It will be a useful tool in wide-ranging *in vivo* electrophysiology experiments including investigating neural correlates of animal behavior.

Limitations of the study

As discussed above, the extracted signals from LFP data are supposed to reflect the head-neck muscular activities surrounding the referenced skull screw. Thus, our current method may not be directly applicable to obtaining activities of other specific

muscles, such as leg[104] or masticatory[105] muscles movements. Implanting and setting a reference electrode into these muscles, although there remains a risk of electrode breakage, has the potential to allow extraction of these muscular activities from LFP data by ICA without additional EMG recording devices.

STAR★METHODS

Detailed methods are provided in the online version of this paper and include the following:

- KEY RESOURCES TABLE
- RESOURCE AVAILABILITY
  - Lead contact
  - Materials availability
  - Data and code availability
- EXPERIMENTAL MODEL AND SUBJECT DETAILS
- METHOD DETAILS
  - Electrode implantation surgery
  - In vivo electrophysiology and behavior experiments
- QUANTIFICATION AND STATISTICAL ANALYSIS
  - Independent component analysis of LFPs
  - Analysis of power spectral density, IC amplitudes, and IC-EMG/EMG amplitudes
  - Behavioral and statistical analysis

SUPPLEMENTAL INFORMATION

Supplemental information can be found online at https://doi.org/10.1016/j.crmeth.2023.100482.

ACKNOWLEDGMENTS

We thank Dr. William Marks for his comments on the manuscript and all other members of the Kitamura laboratory for their support. This work was supported by grants from the Endowed Scholar Program to T.K., the Brain Research Foundation to T.K. (BRFSG-2018-04), the Faculty Science and Technology Acquisition and Retention Program to T.K., the Whitehall Foundation to T.K. (2019-05-38), the National Institute of Mental Health to T.K. (R01MH120134 and R01MH125916), and the Japan Society for the Promotion of Science to H.O. (201860198 and 202101654).

AUTHOR CONTRIBUTIONS

H.O. and T.K. contributed to the study design. H.O. conducted all experiments and analysis. H.O., J.Y., and T.K. contributed to the interpretation for data analysis. H.O. and T.K. wrote the manuscript. All authors approved the final manuscript.

DECLARATION OF INTERESTS

The authors declare no competing interests.

Received: February 24, 2023
Revised: April 12, 2023
Accepted: April 25, 2023
Published: May 17, 2023

REFERENCES

1. Borbély, A.A., Tobler, I., and Hanagasioglu, M. (1984). Effect of sleep deprivation on sleep and EEG power spectra in the rat. Behav. Brain Res. *14*, 171–182. https://doi.org/10.1016/0166-4328(84)90186-4.
2. Vyazovskiy, V.V., Olcese, U., Hanlon, E.C., Nir, Y., Cirelli, C., and Tononi, G. (2011). Local sleep in awake rats. Nature *472*, 443–447. https://doi.org/10.1038/nature10009.
3. Louis, R.P., Lee, J., and Stephenson, R. (2004). Design and validation of a computer-based sleep-scoring algorithm. J. Neurosci. Methods *133*, 71–80. https://doi.org/10.1016/j.jneumeth.2003.09.025.
4. Ji, D., and Wilson, M.A. (2007). Coordinated memory replay in the visual cortex and hippocampus during sleep. Nat. Neurosci. *10*, 100–107. https://doi.org/10.1038/nn1825.
5. Dash, M.B., Douglas, C.L., Vyazovskiy, V.V., Cirelli, C., and Tononi, G. (2009). Long-term homeostasis of extracellular glutamate in the rat cerebral cortex across sleep and waking states. J. Neurosci. *29*, 620–629. https://doi.org/10.1523/JNEUROSCI.5486-08.2009.
6. Kassiri, H., Chemparathy, A., Salam, M.T., Boyce, R., Adamantidis, A., and Genov, R. (2017). Electronic sleep stage classifiers: a survey and VLSI design methodology. IEEE Trans. Biomed. Circuits Syst. *11*, 177–188. https://doi.org/10.1109/TBCAS.2016.2540438.
7. Steenland, H.W., and Zhuo, M. (2009). Neck electromyography is an effective measure of fear behavior. J. Neurosci. Methods *177*, 355–360. https://doi.org/10.1016/j.jneumeth.2008.10.020.
8. Karalis, N., Dejean, C., Chaudun, F., Khoder, S., Rozeske, R.R., Wurtz, H., Bagur, S., Benchenane, K., Sirota, A., Courtin, J., and Herry, C. (2016). 4-Hz oscillations synchronize prefrontal-amygdala circuits during fear behavior. Nat. Neurosci. *19*, 605–612. https://doi.org/10.1038/nn.4251.
9. Isosaka, T., Matsuo, T., Yamaguchi, T., Funabiki, K., Nakanishi, S., Kobayakawa, R., and Kobayakawa, K. (2015). Htr2a-Expressing cells in the central amygdala control the hierarchy between innate and learned fear. Cell *163*, 1153–1164. https://doi.org/10.1016/j.cell.2015.10.047.
10. Okada, S., Igata, H., Sakaguchi, T., Sasaki, T., and Ikegaya, Y. (2016). A new device for the simultaneous recording of cerebral, cardiac, and muscular electrical activity in freely moving rodents. J. Pharmacol. Sci. *132*, 105–108. https://doi.org/10.1016/j.jphs.2016.06.001.
11. Taylor, H., Schmiedt, J.T., Carçak, N., Onat, F., Di Giovanni, G., Lambert, R., Leresche, N., Crunelli, V., and David, F. (2014). Investigating local and long-range neuronal network dynamics by simultaneous optogenetics, reverse microdialysis and silicon probe recordings in vivo. J. Neurosci. Methods *235*, 83–91. https://doi.org/10.1016/j.jneumeth.2014.06.031.
12. Shikano, Y., Sasaki, T., and Ikegaya, Y. (2018). Simultaneous recordings of cortical local field potentials, electrocardiogram, electromyogram, and breathing rhythm from a freely moving rat. J. Vis. Exp., 56980. https://doi.org/10.3791/56980.
13. Zhu, K.J., Aiani, L.M., and Pedersen, N.P. (2020). Reconfigurable 3D-Printed headplates for reproducible and rapid implantation of EEG, EMG and depth electrodes in mice. J. Neurosci. Methods *333*, 108566. https://doi.org/10.1016/j.jneumeth.2019.108566.
14. Whelan, P. (2003). Electromyogram recordings from freely moving animals. Methods *30*, 127–141. https://doi.org/10.1016/s1046-2023(03)00074-4.
15. Liang, Y., Shi, W., Hu, D., Xiang, A., and Zhang, L. (2021). Protocol for recording the discharge of locus coeruleus neurons in free-moving mice during different sleep-wake stages. STAR Protoc. *2*, 100981. https://doi.org/10.1016/j.xpro.2021.100981.
16. Rossetti, N., Luthra, P., Hagler, J., Jae Lee, A.H., Bodart, C., Li, X., Ducharme, G., Soavi, F., Amilhon, B., and Cicoira, F. (2019). Poly(3,4-ethylenedioxythiophene) (PEDOT) coatings for high-quality electromyography recording. ACS Appl. Bio Mater. *2*, 5154–5163. https://doi.org/10.1021/acsabm.9b00809.
17. Buzsáki, G., and Draguhn, A. (2004). Neuronal oscillations in cortical networks. Science *304*, 1926–1929. https://doi.org/10.1126/science.1099745.

18. Steriade, M., McCormick, D., and Sejnowski, T. (1993). Thalamocortical oscillations in the sleeping and aroused brain. Science *262*, 679–685. https://doi.org/10.1126/science.8235588.

19. Buzsáki, G., Leung, L.W., and Vanderwolf, C.H. (1983). Cellular bases of hippocampal EEG in the behaving rat. Brain Res. *287*, 139–171. https://doi.org/10.1016/0165-0173(83)90037-1.

20. Buzsáki, G. (2015). Hippocampal sharp wave-ripple: a cognitive biomarker for episodic memory and planning. Hippocampus *25*, 1073–1188. https://doi.org/10.1002/hipo.22488.

21. Çalışkan, G., and Stork, O. (2019). Hippocampal network oscillations at the interplay between innate anxiety and learned fear. Psychopharmacology *236*, 321–338. https://doi.org/10.1007/s00213-018-5109-z.

22. Pape, H.C., Narayanan, R.T., Smid, J., Stork, O., and Seidenbecher, T. (2005). Theta activity in neurons and networks of the amygdala related to long-term fear memory. Hippocampus *15*, 874–880. https://doi.org/10.1002/hipo.20120.

23. Jones, M.W., and Wilson, M.A. (2005). Theta rhythms coordinate hippocampal-prefrontal interactions in a spatial memory task. PLoS Biol. *3*, e402. https://doi.org/10.1371/journal.pbio.0030402.

24. Kajikawa, Y., and Schroeder, C.E. (2011). How local is the local field potential? Neuron *72*, 847–858. https://doi.org/10.1016/j.neuron.2011.09.029.

25. Liu, A.A., Henin, S., Abbaspoor, S., Bragin, A., Buffalo, E.A., Farrell, J.S., Foster, D.J., Frank, L.M., Gedankien, T., Gotman, J., et al. (2022). A consensus statement on detection of hippocampal sharp wave ripples and differentiation from other fast oscillations. Nat. Commun. *13*, 6000. https://doi.org/10.1038/s41467-022-33536-x.

26. Fein, G., Raz, J., Brown, F.F., and Merrin, E.L. (1988). Common reference coherence data are confounded by power and phase effects. Electroencephalogr. Clin. Neurophysiol. *69*, 581–584. https://doi.org/10.1016/0013-4694(88)90171-x.

27. Jun, J.J., Steinmetz, N.A., Siegle, J.H., Denman, D.J., Bauza, M., Barbarits, B., Lee, A.K., Anastassiou, C.A., Andrei, A., Aydın, Ç., et al. (2017). Fully integrated silicon probes for high-density recording of neural activity. Nature *551*, 232–236. https://doi.org/10.1038/nature24636.

28. Berke, J.D., Okatan, M., Skurski, J., and Eichenbaum, H.B. (2004). Oscillatory entrainment of striatal neurons in freely moving rats. Neuron *43*, 883–896. https://doi.org/10.1016/j.neuron.2004.08.035.

29. Mölle, M., Yeshenko, O., Marshall, L., Sara, S.J., and Born, J. (2006). Hippocampal sharp wave-ripples linked to slow oscillations in rat slow-wave sleep. J. Neurophysiol. *96*, 62–70. https://doi.org/10.1152/jn.00014.2006.

30. Ludwig, K.A., Miriani, R.M., Langhals, N.B., Joseph, M.D., Anderson, D.J., and Kipke, D.R. (2009). Using a common average reference to improve cortical neuron recordings from microelectrode arrays. J. Neurophysiol. *101*, 1679–1689. https://doi.org/10.1152/jn.90989.2008.

31. Nicholson, C., and Freeman, J.A. (1975). Theory of current source-density analysis and determination of conductivity tensor for anuran cerebellum. J. Neurophysiol. *38*, 356–368. https://doi.org/10.1152/jn.1975.38.2.356.

32. Tenke, C.E., and Kayser, J. (2005). Reference-free quantification of EEG spectra: combining current source density (CSD) and frequency principal components analysis (fPCA). Clin. Neurophysiol. *116*, 2826–2846. https://doi.org/10.1016/j.clinph.2005.08.007.

33. Tenke, C.E., and Kayser, J. (2012). Generator localization by current source density (CSD): implications of volume conduction and field closure at intracranial and scalp resolutions. Clin. Neurophysiol. *123*, 2328–2345. https://doi.org/10.1016/j.clinph.2012.06.005.

34. Whitmore, N.W., and Lin, S.C. (2016). Unmasking local activity within local field potentials (LFPs) by removing distal electrical signals using independent component analysis. Neuroimage *132*, 79–92. https://doi.org/10.1016/j.neuroimage.2016.02.032.

35. Bell, A.J., and Sejnowski, T.J. (1995). An information-maximization approach to blind separation and blind deconvolution. Neural Comput. *7*, 1129–1159. https://doi.org/10.1162/neco.1995.7.6.1129.

36. Hyvärinen, A., and Oja, E. (2000). Independent component analysis: algorithms and applications. Neural Network. *13*, 411–430. https://doi.org/10.1016/s0893-6080(00)00026-5.

37. Hyvärinen, A. (2012). Independent component analysis: recent advances. Philos. Trans. A Math. Phys. Eng. Sci. *371*, 20110534. https://doi.org/10.1098/rsta.2011.0534.

38. Jutten, C., and Herault, J. (1991). Blind separation of sources, part I: an adaptive algorithm based on neuromimetic architecture. Signal Process. *24*, 1–10. https://doi.org/10.1016/0165-1684(91)90079-x.

39. Makeig, S., Bell, A., Jung, T.-P., and Sejnowski, T.J. (1995). Independent component analysis of electroencephalographic data. Adv. Neural Inf. Process. Syst. *8*. https://doi.org/10.5555/2998828.2998849.

40. Jung, T.-P., Makeig, S., Humphries, C., Lee, T.W., McKeown, M.J., Iragui, V., and Sejnowski, T.J. (2000). Removing electroencephalographic artifacts by blind source separation. Psychophysiology *37*, 163–178. https://doi.org/10.1111/1469-8986.3720163.

41. Jung, T.-P., Humphries, C., Lee, T.-W., Makeig, S., McKeown, M.J., Iragui, V., and Sejnowsk, T.J. (1997). In Extended ICA removes artifacts from electroencephalographic recordings (MIT Press). https://doi.org/10.5555/3008904.3009029.

42. Vigário, R., Särelä, J., Jousmäki, V., Hämäläinen, M., and Oja, E. (2000). Independent component approach to the analysis of EEG and MEG recordings. IEEE Trans. Biomed. Eng. *47*, 589–593. https://doi.org/10.1109/10.841330.

43. Winkler, I., Haufe, S., and Tangermann, M. (2011). Automatic classification of artifactual ICA-components for artifact removal in EEG signals. Behav. Brain Funct. *7*, 30. https://doi.org/10.1186/1744-9081-7-30.

44. Blanchard, D.C., and Blanchard, R.J. (1972). Innate and conditioned reactions to threat in rats with amygdaloid lesions. J. Comp. Physiol. Psychol. *81*, 281–290. https://doi.org/10.1037/h0033521.

45. Kitamura, T., Saitoh, Y., Takashima, N., Murayama, A., Niibori, Y., Ageta, H., Sekiguchi, M., Sugiyama, H., and Inokuchi, K. (2009). Adult neurogenesis modulates the hippocampus-dependent period of associative fear memory. Cell *139*, 814–827. https://doi.org/10.1016/j.cell.2009.10.020.

46. Kitamura, T., Pignatelli, M., Suh, J., Kohara, K., Yoshiki, A., Abe, K., and Tonegawa, S. (2014). Island cells control temporal association memory. Science *343*, 896–901. https://doi.org/10.1126/science.1244634.

47. Yokose, J., Marks, W.D., Yamamoto, N., Ogawa, S.K., and Kitamura, T. (2021). Entorhinal cortical Island cells regulate temporal association learning with long trace period. Learn. Mem. *28*, 319–328. https://doi.org/10.1101/lm.052589.120.

48. Louie, K., and Wilson, M.A. (2001). Temporally structured replay of awake hippocampal ensemble activity during rapid eye movement sleep. Neuron *29*, 145–156. https://doi.org/10.1016/s0896-6273(01)00186-6.

49. Csicsvari, J., Hirase, H., Czurkó, A., Mamiya, A., and Buzsáki, G. (1999). Oscillatory coupling of hippocampal pyramidal cells and interneurons in the behaving Rat. J. Neurosci. *19*, 274–287. https://doi.org/10.1523/JNEUROSCI.19-01-00274.1999.

50. Tort, A.B.L., Ponsel, S., Jessberger, J., Yanovsky, Y., Brankačk, J., and Draguhn, A. (2018). Parallel detection of theta and respiration-coupled oscillations throughout the mouse brain. Sci. Rep. *8*, 6432. https://doi.org/10.1038/s41598-018-24629-z.

51. Aitken, P., Zheng, Y., and Smith, P.F. (2018). The modulation of hippocampal theta rhythm by the vestibular system. J. Neurophysiol. *119*, 548–562. https://doi.org/10.1152/jn.00548.2017.

52. Vyazovskiy, V.V., and Tobler, I. (2005). Theta activity in the waking EEG is a marker of sleep propensity in the rat. Brain Res. *1050*, 64–71. https://doi.org/10.1016/j.brainres.2005.05.022.

53. Harris, K.D., and Thiele, A. (2011). Cortical state and attention. Nat. Rev. Neurosci. *12*, 509–523. https://doi.org/10.1038/nrn3084.

54. Snipes, S., Krugliakova, E., Meier, E., and Huber, R. (2022). The theta paradox: 4-8 Hz EEG oscillations reflect both sleep pressure and cognitive control. J. Neurosci. *42*, 8569–8586. https://doi.org/10.1523/JNEUROSCI.1063-22.2022.

55. Ward, L.M. (2003). Synchronous neural oscillations and cognitive processes. Trends Cognit. Sci. *7*, 553–559. https://doi.org/10.1016/j.tics.2003.10.012.

56. Funk, C.M., Honjoh, S., Rodriguez, A.V., Cirelli, C., and Tononi, G. (2016). Local slow waves in superficial layers of primary cortical areas during REM sleep. Curr. Biol. *26*, 396–403. https://doi.org/10.1016/j.cub.2015.11.062.

57. Van Gelder, R.N., Edgar, D.M., and Dement, W.C. (1991). Real-time automated sleep scoring: validation of a microcomputer-based system for mice. Sleep *14*, 48–55. https://doi.org/10.1093/sleep/14.1.48.

58. Willie, J.T., Chemelli, R.M., Sinton, C.M., Tokita, S., Williams, S.C., Kisanuki, Y.Y., Marcus, J.N., Lee, C., Elmquist, J.K., Kohlmeier, K.A., et al. (2003). Distinct narcolepsy syndromes in Orexin receptor-2 and Orexin null mice: molecular genetic dissection of Non-REM and REM sleep regulatory processes. Neuron *38*, 715–730. https://doi.org/10.1016/s0896-6273(03)00330-1.

59. Weber, F., Chung, S., Beier, K.T., Xu, M., Luo, L., and Dan, Y. (2015). Control of REM sleep by ventral medulla GABAergic neurons. Nature *526*, 435–438. https://doi.org/10.1038/nature14979.

60. Kocsis, B., Li, S., and Hajos, M. (2007). Behavior-dependent modulation of hippocampal EEG activity by the selective norepinephrine reuptake inhibitor reboxetine in rats. Hippocampus *17*, 627–633. https://doi.org/10.1002/hipo.20299.

61. Brooks, P.L., and Peever, J. (2016). A temporally controlled inhibitory drive coordinates twitch movements during REM sleep. Curr. Biol. *26*, 1177–1182. https://doi.org/10.1016/j.cub.2016.03.013.

62. Peever, J., and Fuller, P.M. (2017). The biology of REM sleep. Curr. Biol. *27*, R1237–R1248. https://doi.org/10.1016/j.cub.2017.10.026.

63. Kayed, K., Hesla, P.E., and Røsjø, O. (1979). The actioculographic monitor of sleep. Sleep *2*, 253–260. https://doi.org/10.1093/sleep/2.2.253.

64. Sridhar, N., Shoeb, A., Stephens, P., Kharbouch, A., Shimol, D.B., Burkart, J., Ghoreyshi, A., and Myers, L. (2020). Deep learning for automated sleep staging using instantaneous heart rate. NPJ Digit. Med. *3*, 106. https://doi.org/10.1038/s41746-020-0291-x.

65. Malafeev, A., Laptev, D., Bauer, S., Omlin, X., Wierzbicka, A., Wichniak, A., Jernajczyk, W., Riener, R., Buhmann, J., and Achermann, P. (2018). Automatic human sleep stage scoring using deep neural networks. Front. Neurosci. *12*, 781. https://doi.org/10.3389/fnins.2018.00781.

66. Cohen, J. (1960). A coefficient of agreement for nominal scales. Educ. Psychol. Meas. *20*, 37–46. https://doi.org/10.1177/001316446002000104.

67. Boyce, R., Glasgow, S., Williams, S., and Adamantidis, A. (2016). Causal evidence for the role of REM sleep theta rhythm in contextual memory consolidation. Science *352*, 812–816. https://doi.org/10.1126/science.aad5252.

68. Aulehner, K., Bray, J., Koska, I., Pace, C., Palme, R., Kreuzer, M., Platt, B., Fenzl, T., and Potschka, H. (2022). The impact of tethered recording techniques on activity and sleep patterns in rats. Sci. Rep. *12*, 3179. https://doi.org/10.1038/s41598-022-06307-3.

69. Terranova, J.I., Yokose, J., Osanai, H., Marks, W.D., Yamamoto, J., Ogawa, S.K., and Kitamura, T. (2022). Hippocampal-amygdala memory circuits govern experience-dependent observational fear. Neuron *110*, 1416–1431.e13. https://doi.org/10.1016/j.neuron.2022.01.019.

70. Debiec, J., and Olsson, A. (2017). Social fear learning: from animal models to human function. Trends Cognit. Sci. *21*, 546–555. https://doi.org/10.1016/j.tics.2017.04.010.

71. Keum, S., and Shin, H.S. (2019). Neural basis of observational fear learning: a potential model of affective empathy. Neuron *104*, 78–86. https://doi.org/10.1016/j.neuron.2019.09.013.

72. Panksepp, J.B., and Lahvis, G.P. (2011). Rodent empathy and affective neuroscience. Neurosci. Biobehav. Rev. *35*, 1864–1875. https://doi.org/10.1016/j.neubiorev.2011.05.013.

73. Fisher, S.P., Godinho, S.I.H., Pothecary, C.A., Hankins, M.W., Foster, R.G., and Peirson, S.N. (2012). Rapid assessment of sleep-wake behavior in mice. J. Biol. Rhythm. *27*, 48–58. https://doi.org/10.1177/0748730411431550.

74. McShane, B.B., Galante, R.J., Biber, M., Jensen, S.T., Wyner, A.J., and Pack, A.I. (2012). Assessing REM sleep in mice using video data. Sleep *35*, 433–442. https://doi.org/10.5665/sleep.1712.

75. Leemburg, S., Vyazovskiy, V.V., Olcese, U., Bassetti, C.L., Tononi, G., and Cirelli, C. (2010). Sleep homeostasis in the rat is preserved during chronic sleep restriction. Proc. Natl. Acad. Sci. USA *107*, 15939–15944. https://doi.org/10.1073/pnas.1002570107.

76. Blaivas, A.J., Patel, R., Hom, D., Antigua, K., and Ashtyani, H. (2007). Quantifying microsleep to help assess subjective sleepiness. Sleep Med. *8*, 156–159. https://doi.org/10.1016/j.sleep.2006.06.011.

77. Bastianini, S., Alvente, S., Berteotti, C., Lo Martire, V., Silvani, A., Swoap, S.J., Valli, A., Zoccoli, G., and Cohen, G. (2017). Accurate discrimination of the wake-sleep states of mice using non-invasive whole-body plethysmography. Sci. Rep. *7*, 41698. https://doi.org/10.1038/srep41698.

78. Pack, A.I., Galante, R.J., Maislin, G., Cater, J., Metaxas, D., Lu, S., Zhang, L., Von Smith, R., Kay, T., Lian, J., et al. (2007). Novel method for high-throughput phenotyping of sleep in mice. Physiol. Genom. *28*, 232–238. https://doi.org/10.1152/physiolgenomics.00139.2006.

79. Mang, G.M., Nicod, J., Emmenegger, Y., Donohue, K.D., O'Hara, B.F., and Franken, P. (2014). Evaluation of a piezoelectric system as an alternative to electroencephalogram/electromyogram recordings in mouse sleep studies. Sleep *37*, 1383–1392. https://doi.org/10.5665/sleep.3936.

80. Flores, A.E., Flores, J.E., Deshpande, H., Picazo, J.A., Xie, X.S., Franken, P., Heller, H.C., Grahn, D.A., and O'Hara, B.F. (2007). Pattern recognition of sleep in rodents using piezoelectric signals generated by gross body movements. IEEE Trans. Biomed. Eng. *54*, 225–233. https://doi.org/10.1109/TBME.2006.886938.

81. Montgomery, S.M., Sirota, A., and Buzsáki, G. (2008). Theta and gamma coordination of hippocampal networks during waking and rapid eye movement sleep. J. Neurosci. *28*, 6731–6741. https://doi.org/10.1523/JNEUROSCI.1227-08.2008.

82. Pompili, M.N., and Todorova, R. (2022). Discriminating sleep from freezing with cortical spindle oscillations. Front. Neural Circ. *16*, 783768. https://doi.org/10.3389/fncir.2022.783768.

83. Khodagholy, D., Gelinas, J., and Buzsáki, G. (2017). Learning-enhanced coupling between ripple oscillations in association cortices and hippocampus. Science *358*, 369–372. https://doi.org/10.1126/science.aan6203.

84. Yamamoto, J., and Tonegawa, S. (2017). Direct medial entorhinal cortex input to hippocampal CA1 is crucial for extended quiet awake replay. Neuron *96*, 217–227.e4. https://doi.org/10.1016/j.neuron.2017.09.017.

85. Vanderwolf, C.H. (1969). Hippocampal electrical activity and voluntary movement in the rat. Electroencephalogr. Clin. Neurophysiol. *26*, 407–418. https://doi.org/10.1016/0013-4694(69)90092-3.

86. Hubbard, J., Gent, T.C., Hoekstra, M.M.B., Emmenegger, Y., Mongrain, V., Landolt, H.P., Adamantidis, A.R., and Franken, P. (2020). Rapid fast-delta decay following prolonged wakefulness marks a phase of wake-inertia in NREM sleep. Nat. Commun. *11*, 3130. https://doi.org/10.1038/s41467-020-16915-0.

87. Adamantidis, A.R., Gutierrez Herrera, C., and Gent, T.C. (2019). Oscillating circuitries in the sleeping brain. Nat. Rev. Neurosci. *20*, 746–762. https://doi.org/10.1038/s41583-019-0223-4.

88. Chen, X., Xu, X., Liu, A., McKeown, M.J., and Wang, Z.J. (2018). The use of multivariate EMD and CCA for denoising muscle artifacts from few-channel EEG recordings. IEEE Trans. Instrum. Meas. *67*, 359–370. https://doi.org/10.1109/TIM.2017.2759398.

89. Mijović, B., De Vos, M., Gligorijević, I., Taelman, J., and Van Huffel, S. (2010). Source separation from single-channel recordings by combining empirical-mode decomposition and independent component analysis. IEEE Trans. Biomed. Eng. *57*, 2188–2196. https://doi.org/10.1109/TBME.2010.2051440.

90. Rejer, I., and Górski, P. (2019). MAICA: an ICA-based method for source separation in a low-channel EEG recording. J. Neural. Eng. *16*, 056025. https://doi.org/10.1088/1741-2552/ab36db.

91. Zou, L., Chen, X., Dang, G., Guo, Y., and Wang, Z.J. (2020). Removing muscle artifacts from EEG data via underdetermined joint blind source separation: a simulation study. IEEE Trans. Circuits Syst. II. *67*, 187–191. https://doi.org/10.1109/TCSII.2019.2903648.

92. Jiang, X., Bian, G.B., and Tian, Z. (2019). Removal of artifacts from EEG signals: a review. Sensors *19*, 987. https://doi.org/10.3390/s19050987.

93. Minguillon, J., Lopez-Gordo, M.A., and Pelayo, F. (2017). Trends in EEG-BCI for daily-life: requirements for artifact removal. Biomed. Signal Process Control *31*, 407–418. https://doi.org/10.1016/j.bspc.2016.09.005.

94. Chen, X., Xu, X., Liu, A., Lee, S., Chen, X., Zhang, X., McKeown, M.J., and Wang, Z.J. (2019). Removal of muscle artifacts from the EEG: a review and recommendations. IEEE Sensor. J. *19*, 5353–5368. https://doi.org/10.1109/JSEN.2019.2906572.

95. Herreras, O., Makarova, J., and Makarov, V.A. (2015). New uses of LFPs: pathway-specific threads obtained through spatial discrimination. Neuroscience *310*, 486–503. https://doi.org/10.1016/j.neuroscience.2015.09.054.

96. Parabucki, A., and Lampl, I. (2017). Volume conduction coupling of whisker-evoked cortical LFP in the mouse olfactory bulb. Cell Rep. *21*, 919–925. https://doi.org/10.1016/j.celrep.2017.09.094.

97. Calderon, D.P., Fremont, R., Kraenzlin, F., and Khodakhah, K. (2011). The neural substrates of rapid-onset Dystonia-Parkinsonism. Nat. Neurosci. *14*, 357–365. https://doi.org/10.1038/nn.2753.

98. McNamara, M., Ersöz, A., and Han, M. (2021). A diagnostic circuit for crosstalk detection in microelectrode arrays. Int. IEEE EMBS Conf. Neural Eng. *2021*, 544–547. https://doi.org/10.1109/ner49283.2021.9441164.

99. Kozai, T.D.Y., Catt, K., Li, X., Gugel, Z.V., Olafsson, V.T., Vazquez, A.L., and Cui, X.T. (2015). Mechanical failure modes of chronically implanted planar silicon-based neural probes for laminar recording. Biomaterials *37*, 25–39. https://doi.org/10.1016/j.biomaterials.2014.10.040.

100. Hara, S.A., Kim, B.J., Kuo, J.T.W., and Meng, E. (2015). An electrochemical investigation of the impact of microfabrication techniques on polymer-based microelectrode neural interfaces. J. Microelectromech. Syst. *24*, 801–809. https://doi.org/10.1109/JMEMS.2015.2434827.

101. Barth, D.S., and Sutherling, W. (1988). Current source-density and neuromagnetic analysis of the direct cortical response in rat cortex. Brain Res. *450*, 280–294. https://doi.org/10.1016/0006-8993(88)91567-3.

102. McFarland, D.J., McCane, L.M., David, S.V., and Wolpaw, J.R. (1997). Spatial filter selection for EEG-based communication. Electroencephalogr. Clin. Neurophysiol. *103*, 386–394. https://doi.org/10.1016/s0013-4694(97)00022-2.

103. Rappelsberger, P., Pockberger, H., and Petsche, H. (1981). Current source density analysis: methods and application to simultaneously recorded field potentials of the rabbit's visual cortex. Pflügers Archiv *389*, 159–170. https://doi.org/10.1007/BF00582108.

104. Zörner, B., Filli, L., Starkey, M.L., Gonzenbach, R., Kasper, H., Röthlisberger, M., Bolliger, M., and Schwab, M.E. (2010). Profiling locomotor recovery: comprehensive quantification of impairments after CNS damage in rodents. Nat. Methods *7*, 701–708. https://doi.org/10.1038/nmeth.1484.

105. Kobayashi, M., Masuda, Y., Fujimoto, Y., Matsuya, T., Yamamura, K., Yamada, Y., Maeda, N., and Morimoto, T. (2002). Electrophysiological analysis of rhythmic jaw movements in the freely moving mouse. Physiol. Behav. *75*, 377–385. https://doi.org/10.1016/s0031-9384(01)00662-x.

106. Delorme, A., and Makeig, S. (2004). EEGLAB: an open source toolbox for analysis of single-trial EEG dynamics including independent component analysis. J. Neurosci. Methods *134*, 9–21. https://doi.org/10.1016/j.jneumeth.2003.10.009.

107. Osanai, H., Kitamura, T., and Yamamoto, J. (2019). Hybrid microdrive system with recoverable opto-silicon probe and tetrode for dual-site high density recording in freely moving mice. J. Vis. Exp. https://doi.org/10.3791/60028.

108. Siegle, J.H., López, A.C., Patel, Y.A., Abramov, K., Ohayon, S., and Voigts, J. (2017). Open Ephys: an open-source, plugin-based platform for multichannel electrophysiology. J. Neural. Eng. *14*, 045003. https://doi.org/10.1088/1741-2552/aa5eea.

109. Amaral-Júnior, P.A., Mourão, F.A.G., Amancio, M.C.L., Pinto, H.P.P., Carvalho, V.R., Guarnieri, L.d.O., Magalhães, H.A., and Moraes, M.F.D. (2019). A custom microcontrolled and wireless-operated chamber for auditory fear conditioning. Front. Neurosci. *13*, 1193. https://doi.org/10.3389/fnins.2019.01193.

110. Makarov, V.A., Makarova, J., and Herreras, O. (2010). Disentanglement of local field potential sources by independent component analysis. J. Comput. Neurosci. *29*, 445–457. https://doi.org/10.1007/s10827-009-0206-y.

111. Schomburg, E.W., Fernández-Ruiz, A., Mizuseki, K., Berényi, A., Anastassiou, C.A., Koch, C., and Buzsáki, G. (2014). Theta phase segregation of input-specific gamma patterns in entorhinal-hippocampal networks. Neuron *84*, 470–485. https://doi.org/10.1016/j.neuron.2014.08.051.

112. Lee, T.W., Girolami, M., and Sejnowski, T.J. (1999). Independent component analysis using an extended infomax algorithm for mixed subgaussian and supergaussian sources. Neural Comput. *11*, 417–441. https://doi.org/10.1162/089976699300016719.

113. Artoni, F., Delorme, A., and Makeig, S. (2018). Applying dimension reduction to EEG data by Principal Component Analysis reduces the quality of its subsequent Independent Component decomposition. Neuroimage *175*, 176–187. https://doi.org/10.1016/j.neuroimage.2018.03.016.

114. Sebek, J., Bortel, R., and Sovka, P. (2018). Suppression of overlearning in independent component analysis used for removal of muscular artifacts from electroencephalographic records. PLoS One *13*, e0201900. https://doi.org/10.1371/journal.pone.0201900.

115. Hyvärinen, A., Särelä, J., Ssrels, J., and Vigário, R. (1999). Spikes and Bumps: Artefacts Generated by Independent Component Analysis with Insufficient Sample Size.

116. Welch, P. (1967). The use of fast Fourier transform for the estimation of power spectra: a method based on time averaging over short, modified periodograms. IEEE Trans. Audio Electroacoust. *15*, 70–73. https://doi.org/10.1109/TAU.1967.1161901.

117. Donoghue, T., Haller, M., Peterson, E.J., Varma, P., Sebastian, P., Gao, R., Noto, T., Lara, A.H., Wallis, J.D., Knight, R.T., et al. (2020). Parameterizing neural power spectra into periodic and aperiodic components. Nat. Neurosci. *23*, 1655–1665. https://doi.org/10.1038/s41593-020-00744-x.

STAR★METHODS

KEY RESOURCES TABLE

REAGENT or RESOURCE	SOURCE	IDENTIFIER
Chemicals, peptides, and recombinant proteins		
DAPI (4′,6-Diamidino-2-Phenylindole, Dihydrochloride)	Thermo Fisher Scientific	Cat#D1306, CAS: 28718-90-3
DiI (DiIC18(3); 1,1′-dioctadecyl-3,3,3′,3′-tetramethylindocarbocyanine)	Biotium	Cat#60010, CAS: 41085-99-8
Experimental models: Organisms/strains		
C57BL/6J	Jackson Labs	Cat#:000664, RRID:IMSR_JAX:000664
Crl:CD1(ICR) (Tg(Sim1-cre)KJ21Gsat/Mmucd)	MMRRC	RRID:MMRRC_034614-UCD
Software and algorithms		
MATLAB 2022a	MathWorks	https://www.mathworks.com/products/matlab.html?s_tid=hp_products_matlab
AnyMaze 7.16	Stoelting	https://www.any-maze.com/
Cheetah 6.4.2	Neuralynx	https://neuralynx.com/software/cheetah
Open Ephys GUI v0.6.1	Open Ephys	https://open-ephys.org/gui
EEGLAB toolbox	Delorme, et al.[106]	https://sccn.ucsd.edu/eeglab/index.php
Custom MATLAB code	This manuscript	https://doi.org/10.5281/zenodo.7859753 https://github.com/HisayukiOsanai/IC-EMG.git
Other		
Silicone probe	NeuroNexus	A1x32-6mm-50-177-H32_21mm
Silicone probe	ATLAS Neuroengineering	E32+R-50-S1-L6 NT
Skull screws (0.80unm x 0.060″ stainless machine screw)	Antrin	https://antrinminiature.com/shop/ols/products/flat-fillister-head-metric-0-dot-80-unm-thread-050-length-stainless-steel-machine-screw
Tungsten wire (0.001″, 50–150 kΩ)	California Fine Wire	CFW0012081
Digital Lynx 4SX	Neuralynx	https://neuralynx.com/hardware/digital-lynx-sx
Open Ephys Acquisition Board	Open Ephys	https://open-ephys.org/acquisition-system/acquisition-board
Head-stage amplifier	Neuralynx	HS-36; https://neuralynx.com/hardware/hs-36
Head-stage amplifier	Intan Technologies	RHD 32; https://intantech.com/RHD_headstages.html?tabSelect=RHD32ch&yPos=100
PFA-coated silver wire, 0.005''	A-M SYSTEMS	Cat#: 786000
Bare silver wire, 0.005''	A-M SYSTEMS	Cat#: 781500
3D Printed Custom-Designed Microdrive	This paper	N/A
Behavior monitoring camera	e-con System	See3CAM_CU55_CHL_TC1
Open field chamber	This paper	N/A
Fear conditioning system	This paper	N/A
Lecia VT1000 S Vibrating Blade Microtome	Leica	VT1000 S
Leica S6E Stereomicroscope	Leica	S6E
Small Animal Stereotaxic Instrument with Digital Display Console	David Kopf Instruments	Model 942
Zeiss AxioImager M2 with Apotome	Zeiss	N/A
Arduino Due	Arduino	https://store-usa.arduino.cc/products/arduino-due?selectedStore=us

RESOURCE AVAILABILITY

Lead contact

Requests for resources and additional information should be directed to and will be fulfilled by the lead contact, Dr. Takashi Kitamura (takashi.kitamura@utsouthwestern.edu).

Materials availability

This study did not generate new unique reagents.

Data and code availability

- All data in the main text or supplementary materials are available upon request.
- The custom MATLAB code used in this study is available at https://doi.org/10.5281/zenodo.7859753 and https://github.com/HisayukiOsanai/IC-EMG.git. The DOI is listed in the key resources table.
- Any additional information required to reanalyze the data reported in this paper is available from the lead contact upon request.

EXPERIMENTAL MODEL AND SUBJECT DETAILS

All procedures relating to mouse care and experimental treatments conformed to NIH and Institutional guidelines, and were carried out with the approval of the UT Southwestern Institutional Animal Care and Use Committee (IACUC). A total of 16 male mice aged between 2 and 10 months were used. Five C57BL/6J background mice were used for open-field recording. Five Crl:CD1(ICR) background mice crossed to C57BL/6J were used both for open-field and fear conditioning recording. An additional two mice Crl:CD1(ICR) in addition to the four C57BL/6J used above were used to record including REM sleep periods (one mouse was also used for open-field/fear conditioning recording). Another four C57BL/6J background mice were used for open-field and observational fear test with four-channel multisite brain areas tungsten electrode implants, from which data were also used in previous studies.[69] All animals were housed on a 12h/12h light schedule.

METHOD DETAILS

Electrode implantation surgery

Fabrication of silicon-probe microdrive and implant surgery was based on a previous report.[107] An implant microdrive equipped with a single-shank 32 channel, 50 μm electrode-site spacing silicon probe (A1x32-6mm-50-177-H32_21mm; NeuroNexus, Ann Arbor, MI, USA; or E32+R-50-S1-L6 NT, ATLAS Neuroengineering, Leuven, Belgium) were prepared for implantation into isoflurane-anesthetized mice. The microdrive was also equipped with a custom-made electric interface board for EMG recording (Figure 1A), which increased the total implant weight to 6.5 g. In the first step, stainless machine screws (Antrin, Fallbrook, CA, USA) were implanted into the skull to anchor the microdrive. One of these skull screws over the center of a cerebellum was attached with bare silver wire, which serves as an electric ground and reference for the LFP recordings (Figure 1B). Electric connectivity was checked by measuring that the impedance is less than 20 kΩ at 1 kHz between the ground screw and other skull screws. The silicon probe was then implanted into hippocampal CA1 and dentate gyrus (DG) (AP: −1.80 mm, ML: +1.60–1.70 mm, DV: +2.10–2.40 mm), then the microdrive was fixed to the skull screws by applying dental acrylic. For the EMG recording, the tips of two perfluoroalkoxy-coated silver wires (A-M Systems, Sequim, WA, USA) were exposed and tied to the left and right dorsal neck muscles (Figure 1C).[7,10] The skin was then covered with dental acrylic.

Implantation of multiple tungsten wire electrodes was reported previously.[69] Briefly, four sets of tungsten wire electrodes were mounted on a custom designed 3D printed microdrive (Figure 5A), which was implanted targeting anterior cingulate cortex (ACC), basolateral amygdala (BLA), white matter above dorsal hippocampal CA1 (WM), and ventral CA1 (vCA1) (ACC: AP: +1.00 mm; ML: −0.30 mm; DV: −1.50 mm, BLA: AP: −1.40 mm; ML: +3.40 mm; DV: −5.30 mm, WM: AP: −2.40 mm; ML: +2.00 mm; DV: −1.00 mm; vCA1: AP: −3.18 mm; ML: +3.75 mm; DV: −4.75 mm). LFP data were re-referenced offline to a skull screw above the cerebellum. All mice were allowed to recover for at least seven days after surgery. All electrode placements were histologically verified with brain slices stained with 4′,6-diamidino-2-phenylindole (DAPI) (Figures 1D and 7B). The probe was coated with 1, 1′-dioctadecyl-3, 3, 3′, 3′-tetramethylindocarbocyanine (DiI) before the implantation.

In vivo electrophysiology and behavior experiments

LFP and EMG signals (Figure 1E) were recorded using Neuralynx (Neuralynx, Bozeman, MT, USA) or Open Ephys (OEPS Tech, Lisbon, Portugal)[108] systems. The wide-band signals were obtained from the implanted electrodes and the EMG wires at 20 kHz, then band-pass filtered (0.1–500 Hz) and down-sampled to 2 kHz.

The LFPs and EMGs of the ten animals were recorded while exploring in the open field chamber (70 cm × 38 cm) for 0.5 to 2 h. Subsequently, five out of the ten animals were recorded during the tone fear conditioning task using a custom-made fear conditioning box.[109] The box consists of a 30 cm × 25 cm × 25 cm transparent acrylic box surrounded by white plastic boards, and 3 mm diameter

stainless steel bars with a 6.66 mm pitch on the floor. Conditioning foot shock (1.2 mA for 20 kΩ impedance) was designed to be delivered to the bars while animal behaviors were monitored with a camera (N660 1080P, NexiGo, Beaverton, Oregon, USA) equipped on the side of the box. Before fear conditioning, all animals were habituated to experimenters for 2 days. On Day1, mice were placed in the fear conditioning box and allowed to explore for 240 s. Then, a 20 s tone (90 dB, 8 kHz) was played from a speaker (ST304, VIP PRO AUDIO, Brooklyn, NY, USA), and a 2-s foot shock was delivered to the mice at the end of the tone, and the animals' behaviors were subsequently monitored for 240 s. This was repeated two more times before the mice were returned to their home cage. On Day2, the mice were placed in the same box but with a different context in the form of black plastic boards on the floor and the surrounding walls. Similarly to day1, the mice explored the box for 240 s, then 20 s tone delivery and 240 s behavior monitoring were repeated in total three times. LFP and EMG were recorded for the whole period of Day2. The timing of the tone and the shock delivery is controlled by the triggering signals of Arduino Due (A000062). The shocker consists of a portable AC power battery (ZeroKor R350), a step-up transformer (Simran AC-100) and a rectifier (KBP210G, Diodes Incorporated, Plano, Texas, USA) for shock delivery, and bipolar transistors (BC547BBU, onsemi, Phoenix, Arizona, USA) and optocouplers (PC817) for shock-timing control. In addition, one mouse used above and two additional mice were recorded in their home cages (18 × 28 × 12 cm) for 4 to 6 h to record LFP data including REM sleep periods.

Another four mice were recorded during the observational fear task in the previous study.[69] Briefly, implanted mice were group housed with their cagemate for one week. On Day1, the implanted mice received one time 0.5 mA, 2-s foot shock (Med Associates, Fairfax, VT, USA). On Day2, the implanted mice and their cagemate were placed in the shock and monitoring chambers, respectively, which were divided by a transparent plexiglass partition. The mice were allowed to explore the chambers for 5 min, then the implanted mice observed the cagemate receiving 0.5 mA, 2-s foot shocks with an interval of 15 s for a total of 24 shock trials). LFPs were recorded from ACC, BLA, WM, and vCA1 during Day2. Due to excessive line and harmonic noises generated during recording in this shock system, we applied notch filters at 60/120/240 ± 0.1 Hz.

QUANTIFICATION AND STATISTICAL ANALYSIS

Unless otherwise noted, analysis of electrophysiological data and animal behaviors as well as statistical analysis were performed using custom written scripts in MATLAB (Mathworks, Natick, MA, USA).

Independent component analysis of LFPs

To the aim of reconstructing EMG signals without direct EMG recording, we performed ICA on LFP data.[34,110,111] Before running ICA, we removed unhealthy channels from the LFP data with two criteria: (1) its waveform is distinct from the neighboring channel (unfunctional channel), (2) the noise level is larger than the other electrode sites that are observable by eye (degraded channel).

To separate source signals from LFP data, we used the infomax ICA algorithm[35,112] which is implemented in the EEGLAB toolbox (*runica.m*).[106] In ICA, the relationship between signal sources and the recorded signals is modeled by

$$\mathbf{x} = \mathbf{A}\mathbf{s}, \quad \text{(Equation 1)}$$

where **x** is the recorded signals, **s** is the source signals called independent components (ICs), and **A** is the unknown mixing matrix which is to be estimated by the ICA algorithms. The source signals are then obtained by the equation

$$\mathbf{s} = \mathbf{W}\mathbf{x}, \quad \text{(Equation 2)}$$

where **W** is computed by the inverse of matrix **A**, which is called unmixing matrix. The number of IC **s** is same with the channel number of the recorded signals **x**. Each column of the mixing matrix **A** describes how the source signals distribute along the original channels, which we called ''weight distribution''. The reconstruction from the *n*'th component onto the original data channels is called inverse ICA, which is accomplished by multiplying the *n*'th column of the mixing matrix **A** with *n*'th IC. For comparing IC's distributions, we normalized their weight distributions so that their maximum absolute is equal to one and their mean value is positive.

Here, we applied ICA to the first 4-min epoch of 32 channel silicon-probe data or previously reported 4 channel tungsten-wire data[69] instead of using the full set of data to reduce the calculation cost. The unmixing matrix **W** was calculated through ICA as described above from the 4-min epoch, and then source signals including outside of the 4-min epoch were obtained using Equation 2. Although data rank reduction using principal component analysis is often applied before ICA, we did not use it because rank reduction can potentially reduce the quality of subsequent ICA.[113] While it is known that too many IC separations can cause overfitting, a problem in which IC waveforms are composed of repeated 'bumps' that do not appear in the original waveforms,[114,115] and indeed we have observed this problem when we have used a 25-μm-spacing 64-ch silicon probe, this overfitting problem was not observed with our recording setups in the current study.

Analysis of power spectral density, IC amplitudes, and IC-EMG/EMG amplitudes

We used Welch's method[116] with a window length of 0.25 s and an overlap of 0.15 s to estimate the power spectral density of EMG and IC. Aperiodic components of the power spectral density were parameterized[117] to help find the spectral peaks. To compare the spectral features of EMG and ICs among different animals, the power spectral densities were normalized by their summation along all frequency ranges.

For evaluating the amplitudes of each IC, we computed how much the ICs account for the original LFP. We calculated the amplitude ratio (Amp. ratio) by the maximum variance of the IC's back-projected (reconstructed) signals among the channels divided by the variance of LFP at the corresponding channel.

To calculate the time-changing amplitudes of the EEG and the EMG components obtained by ICA from LFP (IC-EMG), we first applied the zero-phased band-pass filter (50–500 Hz) to the original waveforms and then their root-mean-squares (RMS) were obtained with 100-ms time windows. Comparisons of RMS among different animals were conducted with z-scored EMG/IC-EMG data.

Behavioral and statistical analysis

During the open-field recordings, the animals' head positions were tracked based on the position of LEDs mounted on the headstage preamplifier. The head position movements were then computed with their average in chunks of every 15 s. The video-based mouse behaviors were categorized as Sleep if the head speed was less than 0.2 cm/s lasting more than 40 s.[73] Animal's awake states were further categorized as Active if the velocity is greater than 2.0 cm/s and as Quiet Awake (QAW) if the velocity is less than 2.0 cm/s in every 15 s epoch.[84] In fear conditioning experiments, animals' freezing behavior was detected by AnyMaze software (Stoelting, Wood Dale, IL, USA). The detection of freezing response during observational fear experiments was carried out using the Video Freeze Fear Conditioning System software (Med Associates) as we previously reported.[69]

To detect REM sleep periods (see Figure 6), theta-to-delta ratio[48,49] and EMG[56–60] amplitude were used in addition to the video-based criteria stated above. First, spectrogram of LFP at CA1 stratum lacunosum-moleculare layer was calculated by continuous wavelet transform with Morse wavelet using *cwt.m* function of MATLAB 2022a. LFPs were separated into 10 s epochs to reduce computational cost for the wavelet transform and subsequently concatenated to calculate theta (6–9 Hz)-to-delta (0.1–4 Hz) ratio. Next, video-based classified Sleep state period were re-classified using IC-EMG/EMG amplitude. The 15 s chunks are further separated into 5 s chunks, then the video-based Sleep was re-classified into QAW if the EMG amplitudes were above z = 1.5 for more than 20% of the chunk duration and otherwise remained into Sleep. Then, Sleep periods were classified into REM if theta-to-delta ratio $\geq$ 4[60] which continues more than 5 s and otherwise into NREM. The short theta-to-delta <4 periods which are <5 s between REM states are also categorized as REM state. Only the mice showing >20 min sleep durations and showing REM states (six mice) were used for the further analysis. Cohen's kappa values was calculated by $\kappa = (p_o - p_e)/(1 - p_e)$,[64–66] where p_o is observed agreement rate between video-based/IC-EMG-based REM periods vs. EMG-based REM periods, and p_e is random agreement rate between them.

We used Student's *t* test after testing normality. Tukey's honest significance tests were employed for multiple comparisons. $p < 0.05$ was assumed to be statistically significant. * indicates $p < 0.05$, ** indicates $p < 0.01$, and *** indicates $p < 0.001$. Detailed statistical analysies are presented in the main text and the figure legends. All tests were two-sided. Bar plots and error bars represent means and standard errors.